AFRL-VS-HA-TR-2006-1100

Characterizing Cirrus Clouds for Their Impact on Airborne Defensive Laser Systems

Donald C. Norquist
Paul R. Desrochers
Patrick J. McNicholl
John R. Roadcap

29 Sep 2006

AIR FORCE RESEARCH LABORATORY
Space Vehicles Directorate
29 Randolph Road
AIR FORCE MATERIEL COMMAND
Hanscom AFB, MA 01731-3010

AFRL-RV-HA-TR-2006-1100

This technical report has been reviewed and is approved for publication.

/signed/
Joel B. Mozer, Acting Chief
Battlespace Environment Division

/signed/ Donald C. Norquist Research Physicist	/signed/ Dwight W. Decker, Chief Space Weather Center of Excellence

Using Government drawings, specifications, or other data included in this document for any purpose other than Government procurement does not in any way obligate the U.S. Government. The fact that the Government formulated or supplied the drawings, specifications, or other data does not license the holder or any other person or corporation; or convey any rights or permission to manufacture, use, or sell any patented invention that may relate to them.

This report is published in the interest of scientific and technical information exchange and its publication does not constitute the Government's approval or disapproval of its ideas or findings.

This report has been reviewed by the Hanscom AFB Public Affairs Office (PA) and is releasable to the National Technical Information Service (NTIS).

Qualified requestors may obtain additional copies from the Defense Technical Information Center (DTIC). All other requestors should apply to the National Technical Information Service (NTIS).

If your address has changed, if you wish to be removed from the mailing list, or if the addressee is no longer employed by your organization, please notify AFRL/RVIM, 29 Randolph Rd., Hanscom AFB, MA 01731-3010. This will assist us in maintaining a current mailing list.

Do not return copies of this report unless contractual obligations or notices on a specific document require that it be returned.

REPORT DOCUMENTATION PAGE

Form Approved
OMB No. 0704-01-0188

1. REPORT DATE *(DD-MM-YYYY)*
29-09-2006

2. REPORT TYPE
Scientific, Interim

3. DATES COVERED *(From - To)*

4. TITLE AND SUBTITLE
Characterizing Cirrus Clouds for their Impact on Airborne Defensive Laser Systems

5a. CONTRACT NUMBER

5b. GRANT NUMBER

5c. PROGRAM ELEMENT NUMBER
621010F

6. AUTHORS
Donald C. Norquist, Paul R. Desrochers, Patrick J. McNicholl and John R. Roadcap

5d. PROJECT NUMBER
1010

5e. TASK NUMBER
0T

5f. WORK UNIT NUMBER
A1

7. PERFORMING ORGANIZATION NAME(S) AND ADDRESS(ES)

Air Force Research Laboratory /RVBYA
29 Randolph Road
Hanscom AFB, MA 01731-3010

8. PERFORMING ORGANIZATION REPORT NUMBER
AFRL-VS-HA-TR-2006-1100

9. SPONSORING/MONITORING AGENCY NAME(S) AND ADDRESS(ES)

10. SPONSOR/MONITOR'S ACRONYM(S)

11. SPONSOR/MONITOR'S REPORT NUMBER(S)

12. DISTRIBUTION/AVAILABILITY STATEMENT
Approved for Public Release; distribution unlimited.

13. SUPPLEMENTARY NOTES

14. ABSTRACT

This study describes the collection of field measurements of cirrus clouds during an eleven-month period over Hanscom AFB, MA, and how those measurements were used to estimate laser transmittance through the cirrus. Using ground-based radar and lidar measurements as a reference, it is shown that radiosonde observations can better detect the presence and geometric attributes of cirrus layers than can geostationary satellites. In comparing satellite retrievals of ice particle size and ice water content with radar/lidar retrievals, the satellite-retrieved effective particle size and ice water content were less than the radar/lidar retrievals. The radar/lidar geometric thickness retrieval of the cirrus is less due to the vertical extent being limited to the higher base and lower top detected by the radar-lidar tandem. Cirrus properties from the case with the smallest optical depth were used in three laser extinction models. Results from all three indicated that a significant power loss occurs as the laser beam propagates through the cloud layer. It seems that knowing cirrus location is more important than knowing the optical properties in laser operations support.

15. SUBJECT TERMS
Laser transmittance, radiosondes, radar and lidar measurments, satellite imagery retrievals, cirrus cloud properties, ice water content, effective particle size, optical depth

16. SECURITY CLASSIFICATION OF:			**17. LIMITATION OF ABSTRACT**	**18. NUMBER OF PAGES**	**19a. NAME OF RESPONSIBLE PERSON**
a. REPORT	**b. ABSTRACT**	**c. THIS PAGE**			Donald C. Norquist
					19B. TELEPHONE NUMBER *(Include area code)*
UNCL	UNCL	UNCL	SAR	72	

Standard Form 298 (Rev. 8/98)
Prescribed by ANSI Std. Z39.18

Contents

APPENDIXES

Illustrations

Tables

Acknowledgements

The authors express their appreciation to the following people for their contribution to the cirrus characterization project:

Radar measurements and analysis – Paul Desrochers, *AFRL/VSBYM*

Radar operations – Kris Robinson, *Utah State University*, Jonathan Blanck and Taylor Harrell, *AFRL/VSB*

Lidar measurements and analysis – Pat McNicholl, *AFRL/VSBYM*, Mitch Laird, *Boston College*

Radiosonde observations – George Clement, *Utah State University*

Forecasting, surface observations – John Roadcap, *AFRL/VSBY*

Satellite imagery analysis – Gary Gustafson, Bob d'Entremont, *AER, Inc.*

FASCODE software adaptation – Jim Chetwynd, *AFRL/VSBYH*

UCLA model code – Steve Ou, *UCLA*

1 INTRODUCTION

Theater ballistic missiles (TBMs) have been used in past regional conflicts involving the U.S. military. Launched by hostile forces from secretive locations, the TBM rises into the upper atmosphere before descending to its target. The rocket engine propelling the missile produces significant radiant energy through boost phase of the flight. This heat signature may be exploited by defensive systems that would direct a high-powered laser beam to the missile fuselage to disable the engine while it is active.

Lasers that are intended for use against military targets are referred to as high energy lasers. A number of different high energy lasers have been envisioned, including land-, sea-, air- and space-based systems. Space-based system concepts suffer from the practical limitation of the huge power requirements of tactical lasers and how such power would be readily supplied on a satellite. Land- and sea-based lasers are expected to be significantly impacted by extinction of the beam due to aerosols and water vapor in the planetary boundary layer. An airborne defensive laser system (ADLS) can largely avoid these limitations if it can loiter at altitudes well above the boundary layer where aerosol and water vapor concentrations are small. Flying at altitudes in the 10-20 km altitude range, the ADLS would be well positioned to engage the TBM during boost phase.

Even at these altitudes, atmospheric phenomena exist that can compromise the amount of laser power that can be placed on a target at some distance from the source. The two major phenomena that have been identified are optical turbulence and ice crystals.

Optical turbulence occurs as small-scale atmospheric density variations that can refract the laser beam, causing it to become more diffuse and less concentrated. Optical turbulence is a term used for small scale spatial and temporal variations in the index of refraction that arise primarily due to small scale variations in atmospheric moisture and temperature. Moisture variations can generally be neglected near and above the tropopause. These fluctuations in index of refraction cause variations in the amplitude, phase, and arrival angle of electromagnetic waves propagating through the atmosphere and can result in degradation to high energy laser systems. Other investigators (Beland, 1993; Jumper and Beland, 2000; Ruggiero et al., 2004; Jackson, 2004) have conducted studies to address this problem.

Ice crystals in cirrus clouds have only recently received attention in regard to their potential impact on ADLSs. As laser beam light photons encounter ice crystals they are scattered and absorbed. Liou et al. (2000) and Ou et al. (2002) have investigated this effect using nominal cirrus cloud characteristics. Their techniques compute the power on the target at any point in its ascent assuming hypothetical source-target engagement scenarios. In their models they account for extinction due to water vapor and dry constituent gas absorption, aerosol extinction, and absorption and scattering due to ice crystals. The latter effect includes single- and multiple-scattering in the forward direction, and backscatter. Besides the direct power, they compute power incident on the target through forward scattering. Their model simulations show that the ice crystal extinction alone could cause significant laser power loss in ADLS transmission in slant paths through nominal cirrus layers for source-target separation distances of 100-200 km. Ice crystal attenuation accounts for a majority of the power loss when a laser beam transits a cirrus cloud, according to their studies.

Numerous investigations of cirrus clouds have been conducted (e.g., Wylie et al., 1994; Wylie and Menzel, 1999; Brown et al., 1995) revealing that cirrus tops can reach tropopause altitudes in both tropical and extratropical regimes. In mid-latitudes, cirrus tops have been measured as high as 15 km from ground-based lidars (Norquist et al., 2003). Sub-visual ice crystal concentrations that may lie above detectable cirrus clouds are essentially unknown. Atmospheric scientists are only beginning to investigate the impact of cirrus on laser transmission.

The purpose of the current project is to determine if cirrus cloud measurements by routine observing systems can provide reliable estimates of cirrus impact on laser transmission. We define “routine observing systems” as surface, upper air and meteorological satellite measurement processes conducted by weather services on a daily basis. If an acceptable level of accuracy is obtained from such systems, the algorithms may be applied to more extensive sets of routine observations to characterize relevant cirrus properties in diverse regions and seasons. Such information may provide valuable guidance for design and deployment of ADLSs.

This project had three major goals. The first goal was to take a series of measurements with routine observing systems and active remote sensors over a wide range of cirrus events. The second goal was to retrieve properties of the cirrus relevant to laser transmission and evaluate their quality. The third goal was to demonstrate the use of retrieved cirrus properties in laser transmission models to estimate their potential impact on ADLS operations.

Section 2 describes the field experiment measurements and the instrument suite used to collect them. Section 3 discusses the algorithms employed in obtaining the cirrus characteristics of interest from the routine observations and from the active remote sensors. In Section 4, the cloud vertical structure and microphysical properties of the observed cirrus clouds are presented. Section 5 demonstrates laser transmission calculations using the cirrus properties, and Section 6 is a discussion of the results and their implications for support to ADLSs.

2 FIELD EXPERIMENT MEASUREMENTS

A series of cirrus-specific cloud measurements were collected at the Hanscom Research Site, Air Force Research Laboratory (AFRL), Hanscom Air Force Base (HAFB), Massachusetts in 2005. Observations were limited to periods where broken or overcast cirrus were expected to be present for at least three hours during a given work day, and where there were no lower clouds or only scattered lower clouds. The three-hour duration requirement helped to insure a temporally consistent cloud configuration so that episodic in-situ observations would be representative of continuous measurements from remote sensors over a period of time. Over 400 ”same-day” and ”next-day” forecasts were issued as guidance over approximately 11 months. The “same-day” forecast was accompanied by a go/no-go decision for the observing equipment operators. During a typical three-hour observing period the co-pointed active remote sensors (cloud radar and lidar) were operated at a fixed near-zenith elevation for at least 30 minutes before a radiosonde was released and a surface observation was taken. Satellite cloud imagery was also collected for the image time closest to but not before the radiosonde launch. The radiosonde was tracked to 20 km altitude. Though all cloud layers observed in the three-hour observing periods were documented, only cirrus layers were analyzed in this study.

The following observing systems and data sources were used in the field experiment observing periods at HAFB that took place in February – December 2005.

a. Air Force Cloud Profiling Radar (AFCPR): This 35-GHz (8.6 mm) Ka-band radar (Desrochers, 2004) operates with a peak power of 1.6 kW and for this project performed cirrus sensing with an average power of 6.5 W. It is designed to provide reflectivity measurements at 75 meter range intervals from all cloud types except those with the smallest particle sizes (e.g., shallow cumulus). Reflectivity measurements were used to determine the altitudes of the base and top of each cloud layer. Because its wavelength is long compared to cloud droplet and crystal sizes (ranging from approximately 1 to 1,000 microns), the AFCPR is less sensitive but also less susceptible to cloud attenuation than a lidar operating at a much shorter wavelength.

b. Portable Electronic Eyesafe Laser (PEELS): This small, eye-safe, direct detection lidar operates at 1.574 μm and 10 Hz pulse repetition frequency to measure backscattered power from detectable targets. It transmits with a signal power of 0.6 W. In optically thick liquid droplet clouds, PEELS experiences significant attenuation, resulting in little penetration by the beam. This is the primary reason that observing days avoided low or middle altitude cloud cover. Because ice clouds are often somewhat transmissive, the PEELS signal can often penetrate and get returns from the entire depth of cirrus layers. As a result, base and top altitudes of the detectable portion of the cirrus layer can be determined. Lidar backscatter power, supplemented by radar reflectivity, was also used to provide estimates of ice crystal size and concentration. In addition, PEELS produces a polarization ratio = depolarized power / polarized power in which purely spherical particles (droplets) have a value near zero and irregular particles (crystals) a larger value. In this way, PEELS can provide guidance to determine the water phase in the cloud layer and insure that only ice clouds were included in the present study.

c. Radiosondes: Balloon-borne Vaisala RS92-SGP Global Positioning System radiosondes were released no sooner than 30 minutes into the three-hour measurement period to coincide with the other measurement systems' operation. They were tracked to an altitude of 20 km. The sondes measure pressure, temperature, humidity, wind speed and direction. These properties provide the atmospheric state for the clear-sky transmission calculation. In addition, as shall be described in the next section, radiosonde pressure, temperature and humidity information was used to make an independent estimate of cloud layer base and top heights.

d. GOES satellite imagery: The National Oceanic and Atmospheric Administration eastern geostationary operational environmental satellite (GOES-12) was the source of cloud imagery for this field experiment. Data for one visible channel and four infrared channels at intervals of about 30 minutes were collected and archived by the AFRL Environmental Satellite Data Facility. The first satellite image collected after the radiosonde launch was used to provide the retrieved cirrus cloud properties (Gustafson and d'Entremont, 2000) used in the laser transmission calculations.

e. Surface observation: HAFB has a Federal Aviation Administration Automated Surface Observing Station (ASOS) near the main runway. However, automated ASOS reports do not report cloud bases higher than 12,000 feet, so they are of limited use for estimating cloud properties. A standard sky condition report (amount of sky cover in eighths and base height in hundreds of feet, including remarks) was taken for each discernable cloud layer at the time of radiosonde launch. PEELS data were often used as guidance for specifying the cloud base height. When few or no lower clouds are present, the human eye can readily detect cirrus in the daylight. Surface observations of sky cover were used to evaluate the cirrus cloud cover as specified by the satellite detection algorithm.

f. Air Force Weather Agency MM5 mesoscale numerical weather model forecast fields for the continental U.S. (CONUS) were obtained for a 15 km grid. A subset of the full grid was extracted that includes HAFB to provide relevant meteorological parameters used in the retrieval of cloud properties from the GOES-12 imagery.

Twenty-six observing periods, in which a total of 28 radiosonde observations (RAOBs) were taken, comprised the field campaign during February – December 2005. Table 1 lists the date and RAOB launch time, the AFCPR/PEELS (radar/lidar, or R/L) observing times, and the GOES imagery times for each of the 28 cirrus observation cases considered in this study. As an example of the data collected, measurements from each observing system are shown for a selected observing period, that of 22 April 2005. Figure 1 shows a time-height cross section of radar reflectivity as measured by the AFCPR. Figure 2 shows the corresponding time-height cross section of detected signal power by PEELS during the same observing period. By comparing the figures, one can readily see that PEELS detects a greater depth of the cirrus layer because of its greater sensitivity to particles the size of ice crystals. However, in cases where the cirrus layer was optically thick, PEELS was more severely attenuated than AFCPR and the radar may detect a higher cloud top. In almost all cases, the base altitude of the (unobscured) cirrus cloud is more accurately discerned from the PEELS measurements. So the AFCPR and PEELS measurements were complimentary, and the lowest base and highest top from the two sensors were always used to specify the reference cirrus altitudes in this study.

Examples of the routine observing system measurements for 22 April 2005 are shown in Figures 3 and 4. Figure 3 shows the analysis of the RAOB launched at 1453 UTC. On the left are temperature and measured relative humidity (with respect to liquid saturation) $\text{RHB}_{\text{waterB}}$ and computed relative humidity (with respect to ice saturation) RHB$_{ice}$B. Depicted at right are wind speed and direction that are measured from sonde locations determined from the Global

Table 1. Hanscom Research Site cirrus cloud field experiment measurements in 2005. All times are UTC.

Date	RAOB Launch Time	R/L Obs Period	GOES Image Time	Cause of Ci
17 Feb	1526	1500 - 1800	1545	front
24 Feb	1656	1200 - 1900	1645	jet stream
22 Apr	1453	1410 - 1800	1515	front
06 May	1145	1100 - 1400	1145	front
20 May	1156	1100 - 1500	1215	front
20 May	1353	1100 - 1500	1415	front
03 Jun	1346	1200 - 1600	1415	front
21 Jun	1505	1400 - 1710	1515	jet stream
24 Jun	1401	1250 - 1620	1415	jet stream
21 Jul	1656	1600 - 1900	1715	convection
26 Jul	1602	1505 - 1805	1615	front
29 Jul	1331	1240 - 1830	1345	front
29 Jul	1644	1240 - 1830	1716	front
08 Aug	1245	1155 - 1500	1315	front
16 Aug	1556	1507 - 1812	1615	jet stream
18 Aug	1146	1100 - 1400	1215	front
19 Aug	1420	1125 - 1525	1445	front
26 Aug	1416	1320 - 1620	1445	front
09 Sep	1149	1055 - 1237	missing	front
30 Sep	1135	1040 - 1515	1145	jet stream
19 Oct	1232	1140 - 1445	1245	jet stream
20 Oct	1339	1255 - 1600	1345	jet stream
21 Oct	1730	1410 - 1930	1740	front
31 Oct	1229	1145 - 1500	1245	jet stream
01 Nov	1914	1655 - 2030	1915	front
09 Nov	1300	1135 - 1500	1315	front
05 Dec	1611	1515 - 1820	1615	jet stream
22 Dec	1514	1420 - 1720	missing	jet stream

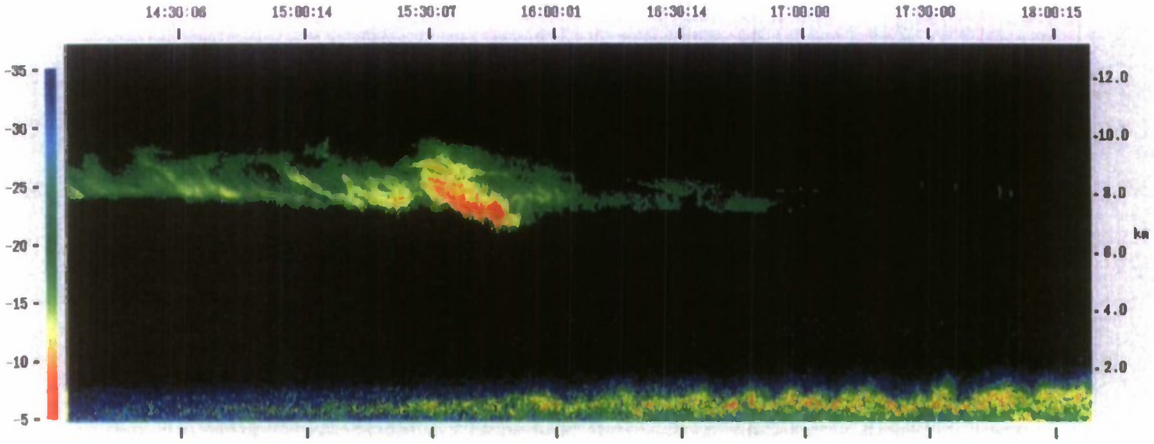

Figure 1. Time- (UTC) height (km AGL) cross section of reflectivity (dBZ) as measured by the 35 GHz Air Force Cloud Profiling Radar (AFCPR) with fixed elevation of 85 degrees, at Hanscom AFB, MA on 22 April 2005.

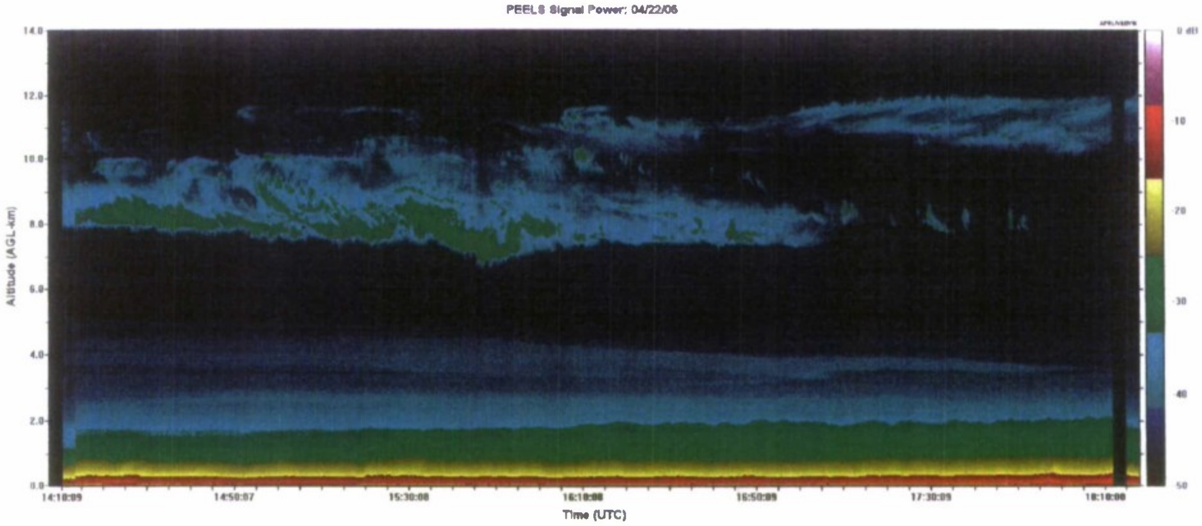

Figure 2. Same as in Figure 1 except for PEELS lidar receiver signal power (dBZ) with a fixed elevation of 85 degrees at Hanscom AFB, MA on 22 April 2005.

Positioning System. Although they were not used in this study, the center section displays the water vapor content and ice water content of an aircraft contrail estimated from the Appleman algorithm (e.g., Schrader et al., 1997). By comparing the left panel of Figure 3 with Figures 1 and 2, we can see a definite altitude coexistence of a maximum of RH_{ice} and an AFCPR and

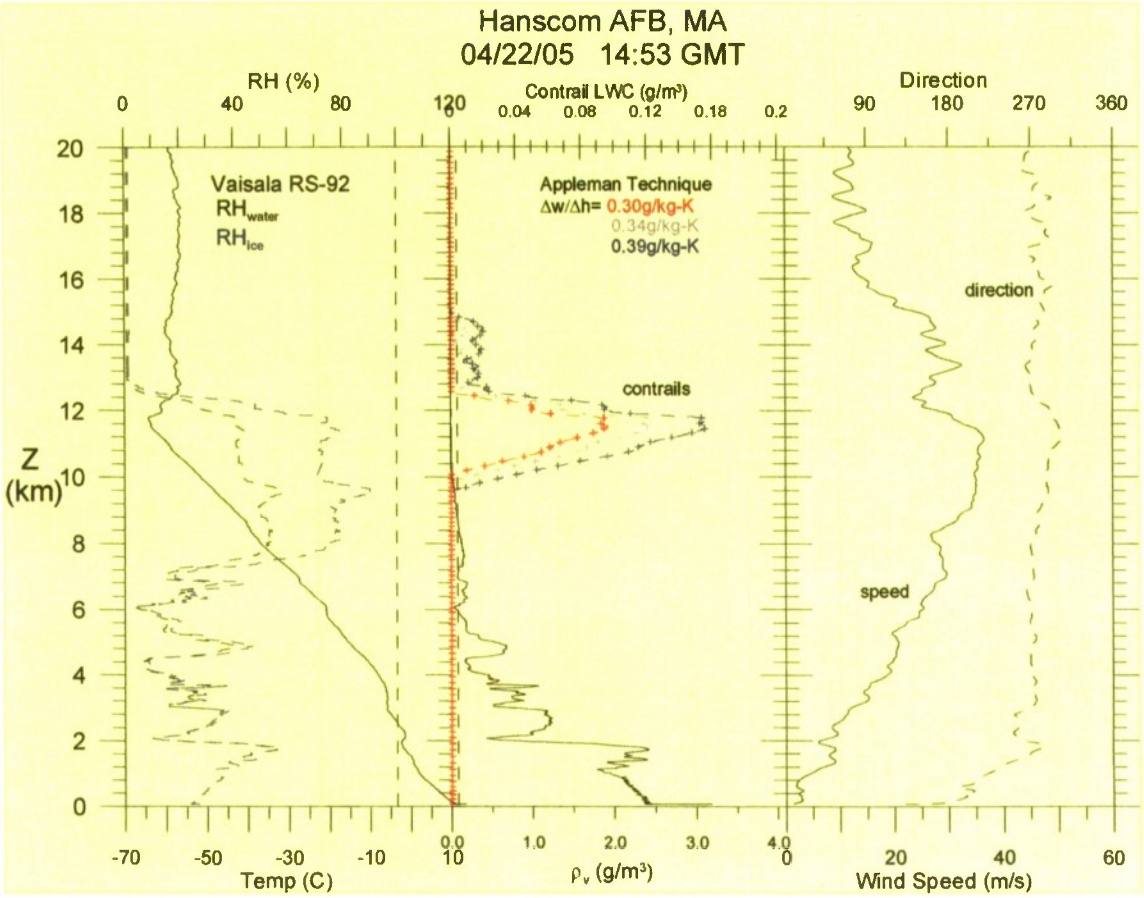

Figure 3. Analysis of Vaisala RS-92 radiosonde observation launched 1453 UTC 22 April 2005 at Hanscom AFB, MA.

PEELS detection of cirrus. In the next section, an algorithm based on this relationship to estimate cloud layer base and top altitude from a RAOB profile is described. Figure 4 shows the GOES-12 image for the 10.7 μm channel for a nominal image time of 1515 UTC. This is one of five channels of GOES-12 data used in the detection of cloud/no cloud (cloud mask) and cloud phase (liquid vs. ice) discrimination in picture elements (pixels) of approximately 5 km on a side. Once the cloud mask and phase are determined for each pixel, an algorithm is employed to retrieve a number of ice cloud properties for ice cloud pixels. These properties include ice water path, 10.7 μm emissivity, effective particle diameter, visible optical depth, cloud top temperature and, with the aid of temperature and geopotential height profiles from MM5 forecast grids interpolated in time to the satellite image time, cloud top and base height. The cloud detection and property retrieval (CDPR) algorithm is described by Gustafson and d'Entremont (2000). Also shown in Figure 4 is the sky condition (cloud) observation taken at the RAOB launch time.

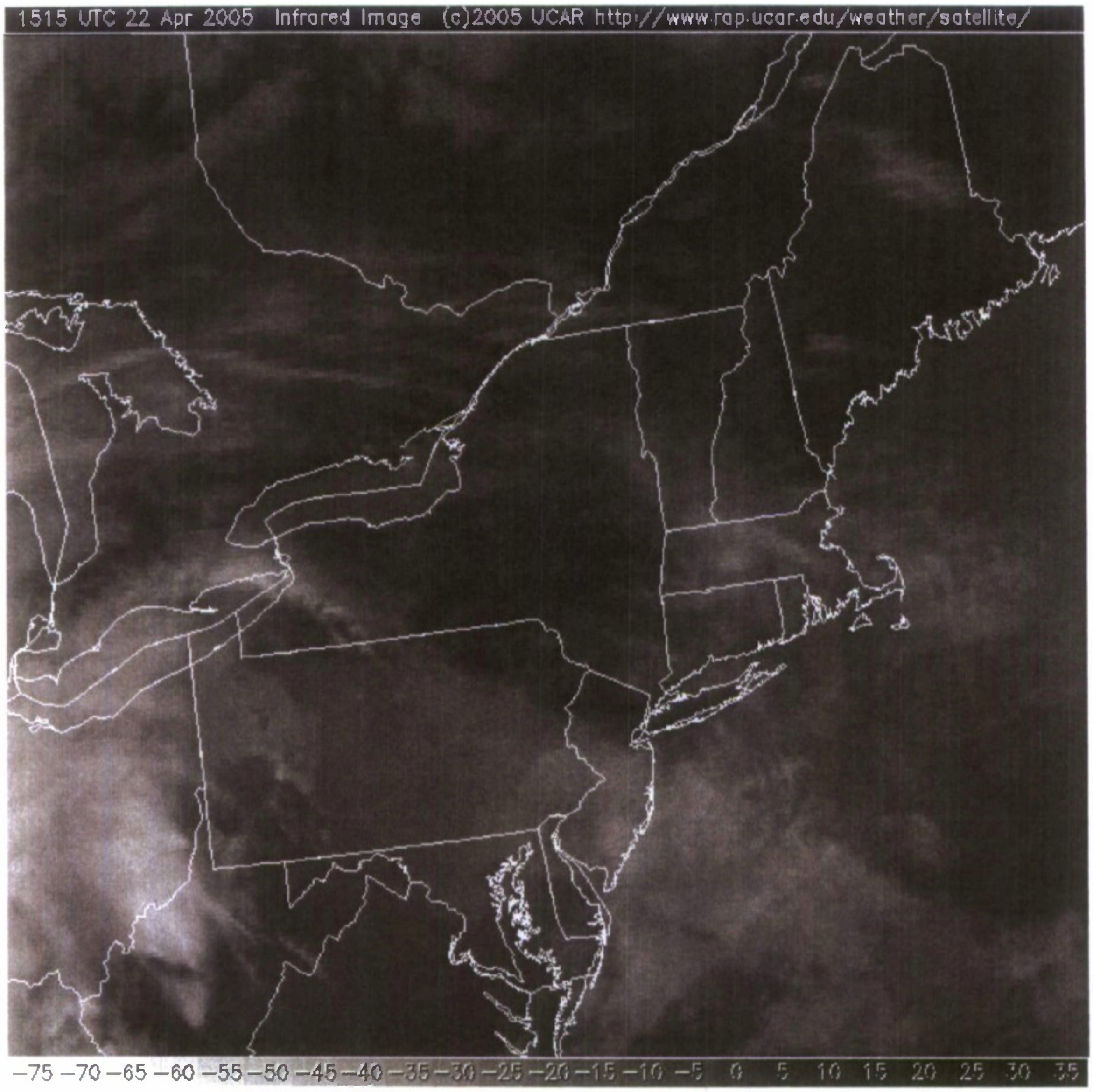

KBED 221453Z VRB04KT 10SM OVC250 12/M07 A3004 RMK AO2 SLP187 T01171072 58004

Figure 4. GOES-12 image from the 10.7 μm channel valid 1515 UTC 22 April 2005. At the bottom of the figure is the surface observation for Hanscom AFB (call sign KBED) valid at 1453, with the original sky cover report (which was CLR) replaced by the surface observer's sky cover report (OVC250).

3 METHODS USED TO DETERMINE RELEVANT CIRRUS PROPERTIES

A major goal of this project was to characterize the properties of cirrus required by laser transmission models to estimate their potential impact on ADLS operations. In particular, cloud base and top altitude (also called cloud vertical structure, or CVS) must be known to place the cloud layer in the actual portion of the atmospheric state profile. The vertical distribution of effective particle size and ice water content is needed to compute the laser extinction coefficient (see for example, Ou et al., 2002) at discrete intervals through the cloud. In the bulk cloud layer approach used in this study, a single value of particle size and water content assumed to be representative of the entire cirrus vertical extent is used to compute extinction coefficient that is applied in each computational interval through the cloud. In this manner, an estimate of laser transmission through the cloud is obtained.

3.1 Determination of Cirrus Cloud Vertical Structure

The reference observations of cirrus CVS used in this study were the radar (AFCPR) and lidar (PEELS) co-pointing measurements of the cirrus layers. They provide accurate specification of cirrus base and top altitude, especially when used together to exploit their complimentary strengths as described in Section 2. Part of the uncertainty in specifying the cirrus CVS from the radar/lidar measurements is in determining the observing time at which the specification should be made. As can be seen in Figures 1 and 2, there is an appreciable temporal variation in the top and base altitude as detected by both the radar and lidar in the observing period. In this study, a printed copy of the radar and lidar images for each observing period was produced. The base and top altitude of the cirrus layer signal as depicted on the images were determined to the nearest 100 m by intersecting lines drawn on the printed images: vertically at the RAOB launch time and horizontally at both the topmost and bottommost cirrus signal indication at that time. These top and base altitudes were then entered into an algorithm, along with the RAOB profile, which estimates the times when the radar/lidar measured the cloud element at which the RAOB entered (t_b) and exited (t_t) the cloud layer. The algorithm takes into account the downwind drift of the sonde and the motion of the clouds due to the winds measured in the sounding. It is described in detail in Appendix 1. Then vertical lines are drawn at times t_b and t_t and the horizontal lines that intersect with them at the altitude position of the radar/lidar signal edge give the wind-corrected base and top cirrus altitudes respectively for both radar and lidar. These times were usually within 15 minutes of the RAOB launch time. The accuracy of this altitude specification is estimated to be approximately ± 200 m. The primary reason for using the sonde entrance and exit times to specify radar/lidar cirrus CVS is for comparison with cirrus CVS as determined from the RAOB, which is described in the following subsection. While the base altitudes were usually in fairly close agreement between the radar and lidar, the lidar tops were generally higher for optically thin clouds and the radar tops were typically higher for optically thick cases. In each observing period, the lower base and higher top were used to specify the reference cirrus CVS.

As stated previously, it was of interest to determine how accurately cirrus CVS could be diagnosed from the routine observations so that cirrus layers could be characterized in the absence of active remote sensors. As mentioned in Section 2, the CDPR algorithm applied to GOES-12 imagery data gives an estimate of cirrus base and top altitudes. But because it is an in-situ instrument, the radiosonde is likely to be more precise in detecting the cloud layer boundaries, especially the cloud base since it is not directly observable from space by a passive sensor.

Several techniques have been developed and employed to estimate CVS from radiosonde soundings. Wang and Rossow (1995) devised and employed a technique that used radiosonde RH to determine CVS for 30 oceanic radiosonde sites over two extended time periods. Wang et al. (1999) used the same technique and evaluated the cloud top and base heights against ground-based remote sensor measurements. Chernykh and Eskridge (1996) used the second derivative of temperature and RH from radiosonde profiles to determine the base and tops of cloud layers present at the time of the sounding. Mozer and Ayer (1998) and Norquist et al. (2003) used fuzzy logic to "fuse" satellite retrieved cloud top height with the radiosonde RH to estimate the probability of cloud at each radiosonde report level. Norquist (2005) evaluated the Wang and Rossow and "fuzzy fusion" techniques on 10 RAOBs for which AFCPR and PEELS measurements of liquid and ice clouds were available for reference. The pre-set RH thresholds in the two schemes led to an excessive number of missed cloud layers and false alarms in comparison to an empirical scheme developed from previous radar/lidar measurements and concurrent RAOBs. Norquist (2005) describes what was referred to as the cloud – meteorological data fusion (CMDF) technique based on this empirical scheme, and augmented by satellite retrievals of top height of the highest cloud layer and a surface observation of the lowest cloud base height.

The CMDF algorithm is described in detail in Appendix 2. Briefly, concurrent radar/lidar CVS specifications of observed cloud layers and RAOB soundings of those cases are combined to form an empirical relationship between cloud probability and relative humidity [CP = f(RH)] that can be applied to independent sounding data to estimate CVS. The relationships were developed separately for three temperature regimes: T ≥ 0 C, 0 C > T > -40 C, and T ≤ -40 C. The relationships are then applied to independent sets of RAOBs for which satellite retrievals and surface observations are available. If the satellite imagery cloud mask detects ice cloud within a preset distance of the RAOB launch site and maximum diagnosed CP in the temperature regime T ≤ -20 C is less than 0.51, then the ice cloud is "dubbed in" by setting CP = 0.51 for sounding levels centered on the maximum CP level and no more than ±1000 m above and below it. A similar augmentation of computed CP values is employed if low or middle cloud is detected by satellite or surface observation and no CP values of greater than 0.51 are diagnosed for T ≥ -5 C. In this case, the dubbed cloud layer is limited to no more than 1000 m thick, centered on the maximum CP level in this temperature regime. If a surface observation by a human observer reports clear skies, CP is set to 0.25 at all levels. Similarly, if CP is diagnosed to be ≥ 0.51 at levels above the tropopause as defined by the method of Roe and Jasperson (1980), then these levels are set to 0.25 to limit the cirrus to the troposphere.

The CMDF algorithm provides an estimate of the cloud probability (CP) at each report level in the manner described in Appendix 2 and summarized above. All levels determined to have CP ≥ 0.51 are considered cloudy, and cloud layer top and base heights are chosen to be the highest and lowest such level in a layer at least 100 m thick. Diagnosed cloud layers must be separated by at least 500 m or they are considered a single layer. In the current study, 19 previous (Vaisala RS80) RAOB, AFCPR and PEELS multiple cloud layer measurement cases involving high, middle and low cloud types were used to develop the CP=f(RH) relationships. The relationships were applied to the 28 (Vaisala RS92-SGP) RAOBs in this project in the CMDF algorithm. Since the focus of this study is on cirrus clouds, only the resulting diagnosed cirrus layers were analyzed. Satellite-retrieved cirrus top altitudes (when detected) and human surface observations of the cirrus were available for augmenting the CP profiles when cirrus was not diagnosed. However, all observed cirrus layers were diagnosed in the CP=f(RH) relationships applied to the RAOBs. The cirrus CVS from the CDPR (satellite-based) and CMDF (RAOB-based) algorithms are compared with reference radar/lidar CVS in Section 4.

3.2 Determination of Cirrus Microphysical Properties

Airborne cloud particle probes are considered the most accurate systems for measuring the particle size distributions of cirrus clouds. These systems include forward scattering spectrometer probes for measurement of the smallest particles, and one- and two-dimensional optical array probes for the medium and largest ice particle sizes. Many field experiments have been conducted to make these in-situ cirrus measurements, including those described by Heymsfield and Platt (1975) and McFarquhar and Heymsfield (1996).

In-situ cirrus particle measurements were not available in the field experiment conducted for the current project. Instead, the microphysical properties required by the laser transmission models were retrieved from the PEELS and AFCPR measurements using the technique of Donovan and van Lammeren (2001) and from the satellite imagery by the CDPR algorithm. Both retrieval schemes make a number of assumptions about ice particle shapes and size distributions. The CDPR algorithm was used as is, but the radar/lidar retrieval scheme was modified to account for the AFCPR and PEELS wavelengths. A gamma value of 5 was used for the particle size distribution, and the scheme was executed in single scattering mode. Because both retrievals are estimates from remote sensors, the radar/lidar specifications cannot be considered a "reference" for a conclusive evaluation of the satellite estimates of the microphysical properties. In-situ data are required for such a reference.

The digitized PEELS backscatter power and AFCPR reflectivity measurement data were processed in a manner to make them time-coincident for input to the retrieval method. Time series of the lidar backscatter power (in 100 kmP^{-1P} srP^{-1P}) and radar reflectivity (in mmP^{-6P} mP^{-3P}) at their respective range gates were presented to the retrieval technique along with the RAOB profile. These are shown in Figure 5 for the 5 December 2005 observing period. The retrieval scheme was then executed to produce an estimate of effective particle radius (rB$_{\text{effB}}$) and ice water content (IWC) at each range gate and measurement time for which the lidar backscatter power and radar reflectivity was non-zero.

In order to allow comparison with satellite-based retrievals of the bulk microphysical properties, a vertical average of the rB$_{\text{effB}}$ and IWC was computed. These were averaged over a 10-minute period beginning with the

"GOES Image Time" as shown in Table 1. These vertical-time averaged bulk properties are reported in Section 4 and used in the calculations described in Section 5 to represent the radar/lidar estimates of cirrus extinction.

Cirrus properties retrieved by application of the CDPR algorithm (Gustafson and d'Entremont, 2000) to satellite imagery were listed in Section 2. The retrieved bulk microphysical properties required by the laser transmission model are the effective particle diameter (DB$_{effB}$) and ice water path (IWP). These properties are estimated in a simultaneous retrieval scheme that includes the estimation of cirrus radiance temperature, long-wave (10.7 µm) emissivity and visible wavelength optical depth. The retrieval scheme is described in detail by Gustafson and d'Entremont (2000). However, it is important to note that the microphysical property estimates are only available for satellite imagery pixels where cloud was specified by the cloud detection algorithm and the phase discrimination process determined it to be ice particles. The detection and phase discrimination techniques are detailed by Gustafson and d'Entremont (2000).

In this study, all of the cirrus properties retrieved by the CDPR algorithm for ice cloud pixels within a 28 km radius of the RAOB launch site were averaged for the GOES-12 image time closest to but not before the RAOB launch time. These average values were reported (Section 4) and used in a demonstration of the laser transmission models (Section 5). The 28 km radius for averaging was determined from a nominal cirrus altitude of 10 km AGL and an elevation angle of 20° to define the celestial dome for the surface observer. This also allows for a qualitative comparison of the cirrus coverage (fraction of pixels in the radius for which ice cloud was specified in the CDPR algorithm) with sky cover recorded by the surface observer at launch time. The presence of cirrus in at least one pixel was required in this study for the cirrus to be considered "detected" by the CDPR algorithm. In such cases, resulting CVS and microphysical properties were evaluated in Section 4 and used in laser transmission calculations as reported in Section 5.

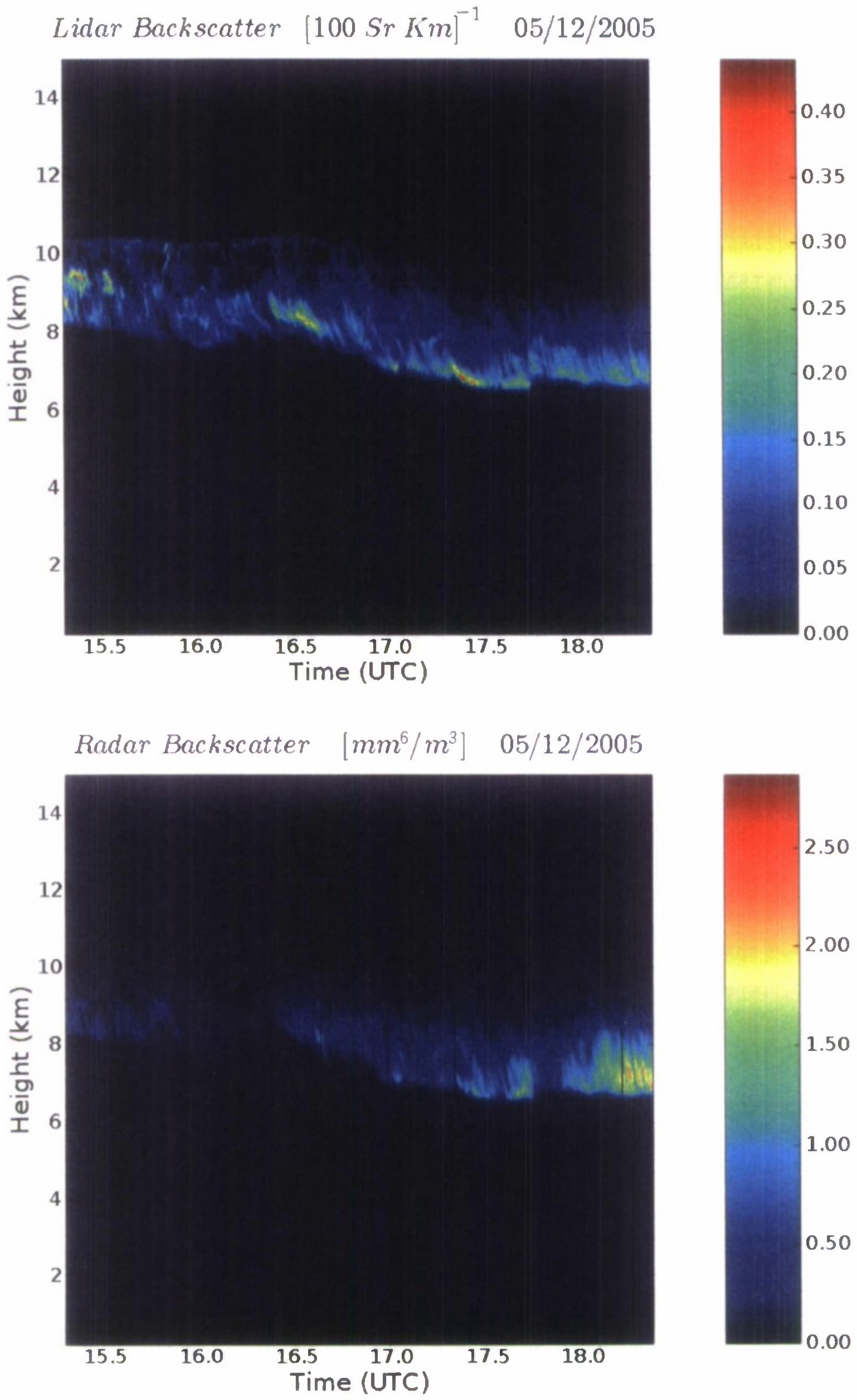

Figure 5. Lidar backscatter and radar reflectivity for 5 December 2005.

4 CIRRUS CHARACTERIZATION RESULTS

In this section the results of the specification of cirrus CVS from the routine observing systems are compared with those of the reference observing systems. Retrievals of microphysical properties from satellite imagery are presented for all observing periods for which cloud was detected, and from the ground-based remote sensors for selected observing periods for comparison with the satellite-based retrievals.

4.1 Cirrus Cloud Vertical Structure Results

Figures 6 and 7 present a visual summary of the cirrus CVS comparison results. In Figure 6, the tropopause level diagnosed from the RAOB for each sounding is shown as an additional reference. It is difficult to assign a level of accuracy to the diagnosed tropopause because of the differences in how it is defined. It is clear from Figure 6 that, in a majority of the observing periods, the radar/lidar depiction of cirrus top altitude was higher than the tropopause. It is commonly accepted that the tropopause acts as an upper limit for the altitude of non-convectively generated cirrus clouds. This apparent discrepancy is probably due more to the uncertainty in assigning the tropopause than it is the uncertainty of the radar/lidar top cirrus top height measurement. But the uncertainty remains: is it possible that the height of stratiform cirrus can exceed the tropopause altitude? Resolution of this question is beyond the scope of this study. Despite this uncertainty, the diagnosed tropopause was used to cap the CMDF-diagnosed cirrus layer.

Generally, the R/L cirrus top follows the tropopause height variation with calendar date – higher in the warm months, lower in the cold seasons. However, in an appreciable number of observing periods (25%), the R/L cirrus top height lies well below the diagnosed tropopause. This challenges previous assumptions that the tropopause can be used as a reliable estimate for the cirrus layer top height. The six observing periods from 20 May to 26 July show that a significant amount of variation is possible in the cirrus top height, much more so than in the tropopause altitude for the same period. Interestingly, the variation is evident in the CMDF-diagnosed

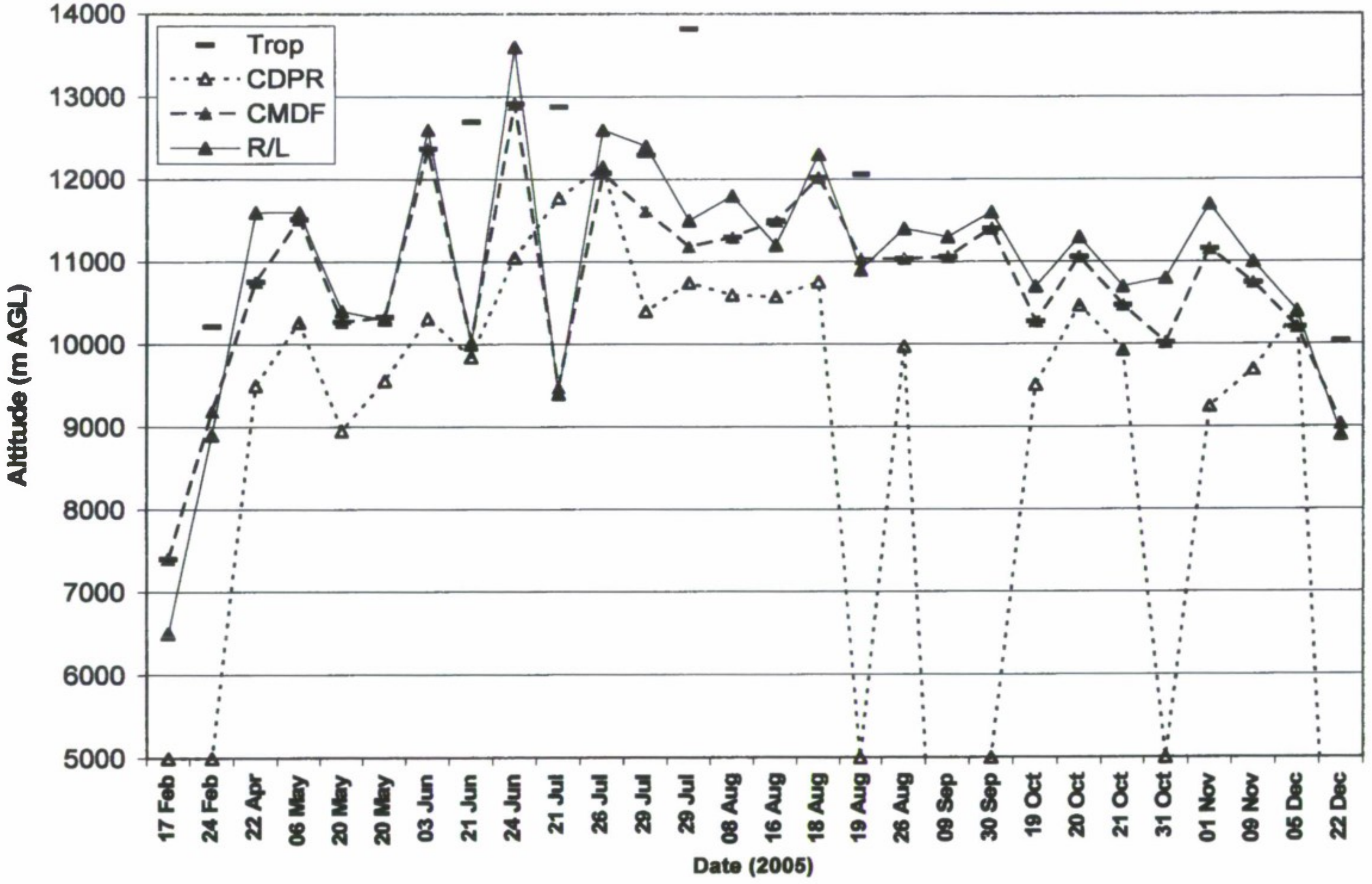

Figure 6. Diagnosed (CDPR algorithm, CMDF algorithm) and measured [radar/lidar (R/L)] cirrus layer top altitude for the 28 RAOB soundings. Cirrus undetected by CDPR are shown as 5000 m. Tropopause (Trop) is derived from RAOB data.

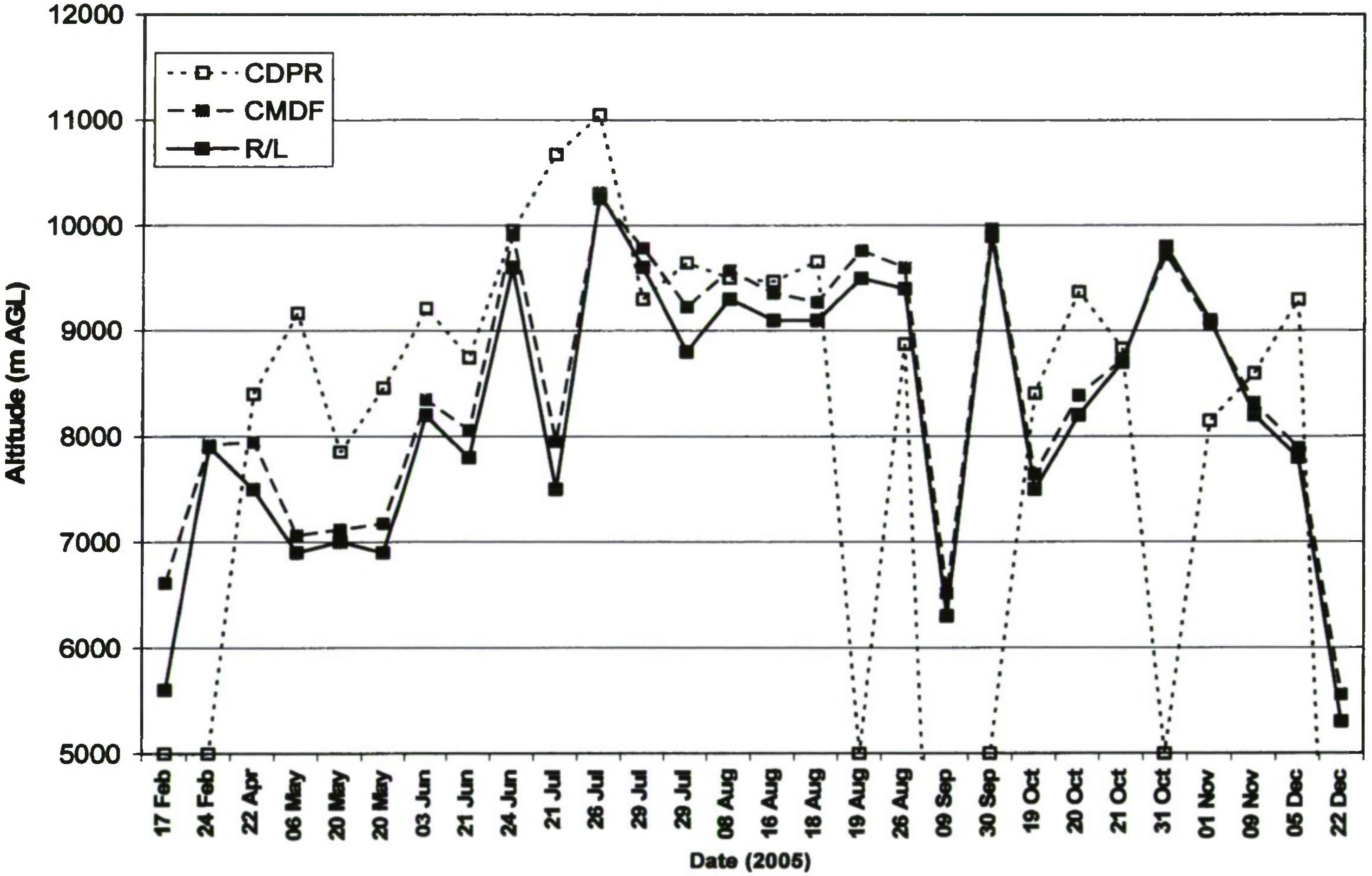

Figure 7. Same as in Figure 6, except diagnosed (CDPR algorithm, CMDF algorithm) and measured [radar/lidar (R/L)] cirrus layer base altitude for the 28 RAOB soundings. Cirrus undetected by CDPR are shown as 5000 m.

cirrus top height, but is not present in the CDPR-retrieved cirrus top altitude. In fact, the CMDF top height rises and falls with the reference cirrus top altitude over most of the field experiment period with the exception of 16 Aug, 9 Sep and 31 Oct.

The CMDF algorithm, and in particular the CP=f(RH) relationship, did not fail to diagnose cirrus in a single observing period. This means that it has a probability of detection (POD) of one. This is in contrast to the satellite-based CDPR retrieval, which did not detect cirrus (within 28 km of the RAOB launch site) in five cases of observed cirrus. This suggests that the RS92 radiosonde has the capability to detect even thin cirrus missed by the cloud detection algorithm applied to GOES imagery. However, a qualification to these statements is in order. First, only days with observed cirrus were used as observing periods, so the ability of the CMDF algorithm to avoid false alarms (diagnosing non-existent cirrus) is unknown from the cases considered in this study. Norquist (2005) showed that in 10 observing periods in which a distinct cirrus layer was present in five, the CP=f(RH) relationship diagnosed four of the cases. But it also diagnosed non-existent cirrus in two observing periods. What was found in those cases is that the radiosonde-based algorithm might detect a moist layer and assign CP ≥ 0.51 when it was not yet near enough saturation (with respect to ice) to evidence visible cirrus. Another important qualification is that even though the CDPR algorithm did not detect cloud at the time nearest/following the RAOB launch, it may have detected cirrus in subsequent 30-minute interval images. In general, as cirrus moved into or formed in the viewing area, the lidar was the first to detect it, followed by the radar as it thickened and then by the satellite detection as it thickened further.

In Figure 7 we see a similar relationship between CDPR retrieved cirrus base altitude, CMDF diagnosed cirrus base height and R/L reference cirrus bases. The case-to-case variation of the CMDF base heights follows that of the R/L, with only two exceptions (22 Apr and 20 May). CDPR retrieved base height has temporal trends that are essentially uncorrelated with the R/L trends. It should be expected that an in-situ sensor, even one that does not explicitly sense cloud particles, should be more accurate specifying cloud boundaries than a space-based passive remote sensor. In fact, it is remarkable that the CDPR algorithm performs as well as it does, especially in retrieving cloud base height.

Statistics of the comparison of CDPR and CMDF cirrus top, base and thickness estimates with the R/L measurements are shown in Table 2. There are a few notable characteristics of the comparison statistics that are instructive. First, there is a significant negative bias in the CDPR specification of cirrus top height. At least part of the CDPR top underestimate is due to the fact that the maximum emission sensed by the satellite instruments does not come from the boundary between the ice crystals and the cloudless air (what we would think of as the "top"). Instead, it comes from some point down into the cirrus mass of crystals where the particle concentration is sufficient to both absorb the upwelling radiation from below and emit a sufficiently strong signal to space. It is the temperature at this altitude that determines the radiance sensed at the satellite. Supporting this notion is the fact that, in all but one of the 21 observing periods in which CDPR top height was evaluated, it was assigned lower than the R/L reference top height. How far down into the cloud this level is is uncertain. Two factors contribute: the vertical variation of the ice water content and the vertical variation of the ice crystal size. Ice mass varies with the water vapor distribution, commonly (but not necessarily) greatest near the middle of the cloud layer. Crystal size tends to increase with temperature (Gustafson and d'Entremont, 2000) and smaller particles are less transmissive of the near infrared wavelengths sensed by the satellite instruments. This latter factor might place the source of the sensed radiation near the cloud top. The two factors together would suggest that the radiation emission height is in the upper half of the cirrus layer. Sometimes this height is called the "radiative" height rather than the top height.

The retrieved cloud top temperature from the CDPR algorithm, which is used to determine the CDPR cloud top height (by means of the MM5

Table 2. Statistics from the comparison of the CDPR algorithm and CMDF algorithm diagnosis of cloud top height, cloud base height and consequent depth of the observed cirrus layer with corresponding AFCPR/PEELS radar/lidar cirrus layer measurements. Statistics include bias, mean absolute error (MAE) and standard deviation of the error (St Dv). Values are shown for the 21 cases in which CDPR detected cirrus as shown in Figures 6 and 7, and for all 28 observing periods. All units are meters.

	Cirrus Layer Top			Cirrus Layer Base			Cirrus Layer Depth		
	Bias	MAE	St Dv	Bias	MAE	St Dv	Bias	MAE	St Dv
CDPR-21	-1085	1312	1071	767	936	909	-1852	1852	816
CMDF-21	-294	336	364	199	206	139	-493	497	312
CMDF-28	-212	348	378	212	223	208	-424	446	328

height/temperature profiles), was compared with the temperature at the height of the top and base of the cloud layer as determined from the radar/lidar. For the 21 cases of CDPR retrievals, the CDPR cloud top temperature average was 226.4 K, compared with R/L cirrus top and base average temperatures of 218.1 and 240.4 K respectively. Thermally, this is in the upper half of the cloud layer.

As for the CMDF top estimates, the tropopause estimate constrained the cirrus top assignment to be at or below the level of the R/L top in 20 of the 28 cases. Part of the negative bias in the tropopause-constrained CMDF top estimates is due to the uncertainty of the relative position of the tropopause and the R/L top height as discussed earlier. The constraint is actually beneficial to the performance of the CMDF algorithm, because without it the top height bias becomes positive at 410 m – a positive bias in 26 of 28 cases. This suggests that the threshold RH for cloud indication (CP = 0.51) may be too low for the relatively cold temperatures at above-cirrus altitudes. No improvement of this bias was seen when a subset of 21 of the 28 cases were used to develop RS92 CMDF coefficients, which were then applied to the remaining seven RAOBs.

Both the satellite and RAOB algorithms overestimate the base height, with the latter to a much lower degree. The CDPR layer depth was computed to be exactly 1100 m in all of the 21 cases. On average, this resulted in a CDPR-retrieved cirrus layer that was 1852 m thinner than the reference R/L cirrus layer. It is obvious that in this application of the CDPR algorithm, a default thickness value was used to specify the base height. In terms of mean absolute error (MAE), the CMDF base estimate was even more accurate than the CMDF top determination. Like the unconstrained CMDF top height, the base height estimate was consistently (in all but two observing periods) higher than the R/L value. But because the R/L value is estimated to have the same MAE (± 200 m), it is not clear if this is a real systematic error. CMDF base height positive bias improved slightly when using the RS92 coefficients on the seven independent RAOBs.

4.2 Cirrus Cloud Cover Results

The areal coverage of cirrus can be a factor influencing the choice to operate an ADLS. In cases of scant or even scattered coverage, the probability of encountering cirrus in the laser path may be low enough to warrant deployment. Therefore, it is of interest to determine how accurately the CDPR algorithm determines cirrus coverage. As mentioned previously, in the cloud mask a pixel is declared clear, liquid cloud filled or ice cloud filled. In the celestial dome estimated to have a radius of 28 km for this project, roughly 100 pixels were considered. The fraction determined to be ice cloud filled was used as the cirrus coverage, and the cirrus properties (both CVS and microphysical) retrieved for all such pixels were averaged to provide the CDPR algorithm values reported. Surface observations of cirrus coverage in eighths of sky cover by a human observer serve as a reference for the CDPR coverage.

Figure 8 is a plot of the fractional cirrus coverage as determined by the CDPR algorithm and by the surface observer for the 26 cases for which satellite imagery were available. Also shown is the CDPR estimate of long-wave (10.7 μm) emissivity averaged over all pixels specified as ice cloud filled. The emissivity indicates how nearly the cirrus absorbs and emits radiation of this wavelength as a black body (having an emissivity of one). Because a cirrus cloud with a high emittance would be easier to detect than one with a low emissivity,

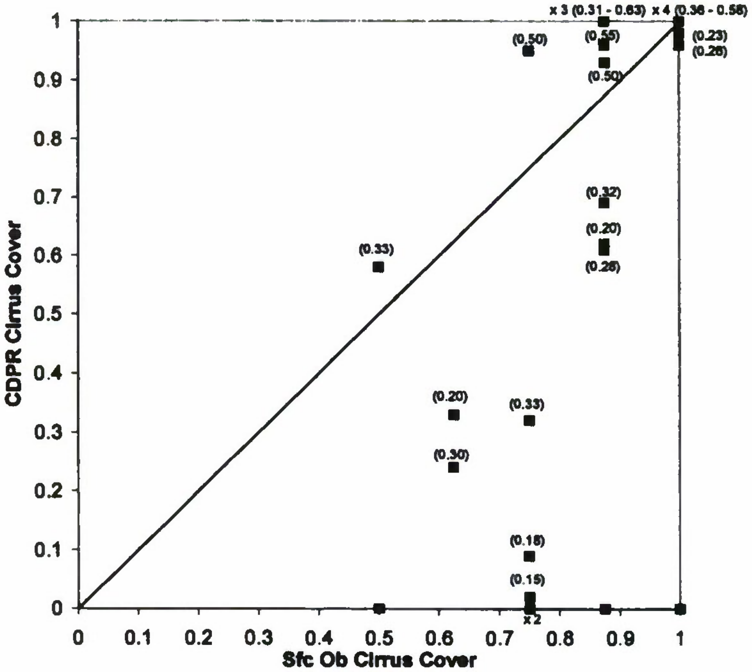

Figure 8. Scatter plot of cirrus cover as detected by the CDPR algorithm and as observed by a surface observer. Long-wave (10.7 μm) emissivity as retrieved by the CDPR algorithm is shown in parentheses for each plotted point.

the average emissivity of the ice cloud pixels in an area might be positively correlated with the cirrus coverage in the area. We see from Figure 8 that there is a tendency, with exceptions, toward larger emissivity when CDPR cirrus coverage is greater. We also see that, in observing periods where less than 7/8 cirrus coverage was observed from the ground, the CDPR coverage tended to be underestimated. The extreme cases of this underestimation were the five observing periods where no cirrus were detected in the observing area in the satellite image at or immediately following RAOB launch.

4.3 Cirrus Cloud Microphysical Results

Gustafson and d'Entremont (2000) describe a scheme in which several microphysical and optical properties are retrieved simultaneously. These include radiative temperature, visible optical depth, long-wave emissivity, effective particle diameter and ice water path. These along with the cloud top height set by the radiative temperature using the temperature/height profile from the nearest MM5 grid point and an estimate of the cloud base height constitute the retrieved parameters. Because the focus of this study is on the impact of ice clouds on laser transmission, the analysis concentrates on the two bulk parameters instrumental in its determination: DB_{effB} and IWP. CDPR retrieved DB_{effB} and IWP are shown for the 26 cirrus cloud cases in Figure 9.

The microphysical retrievals from the radar and lidar reflectivity/backscatter power measurements were conducted for a selected subset of the observing periods. Those events in which few or no liquid clouds were observed during the three-hour period were selected to minimize complications with the newly implemented retrieval algorithm of Donovan and van Lammeren (2001). Time-altitude images of the IWC and rB_{effB} are shown for the 5 December 2005 observational period in Figure 10. Bulk values of IWC (converted to IWP) and rB_{effB} (converted to DB_{effB}) are shown in Table 3 along with the corresponding satellite-based retrieved properties for GOES-12 image times as indicated in Table 1 during the selected observational periods. The radar/lidar retrieved IWC was converted to IWP by multiplying the bulk (vertical average) IWC by the retrieved cirrus layer thickness. Radar/lidar retrieved rB_{effB} was doubled for comparison with satellite retrieved DB_{effB}.

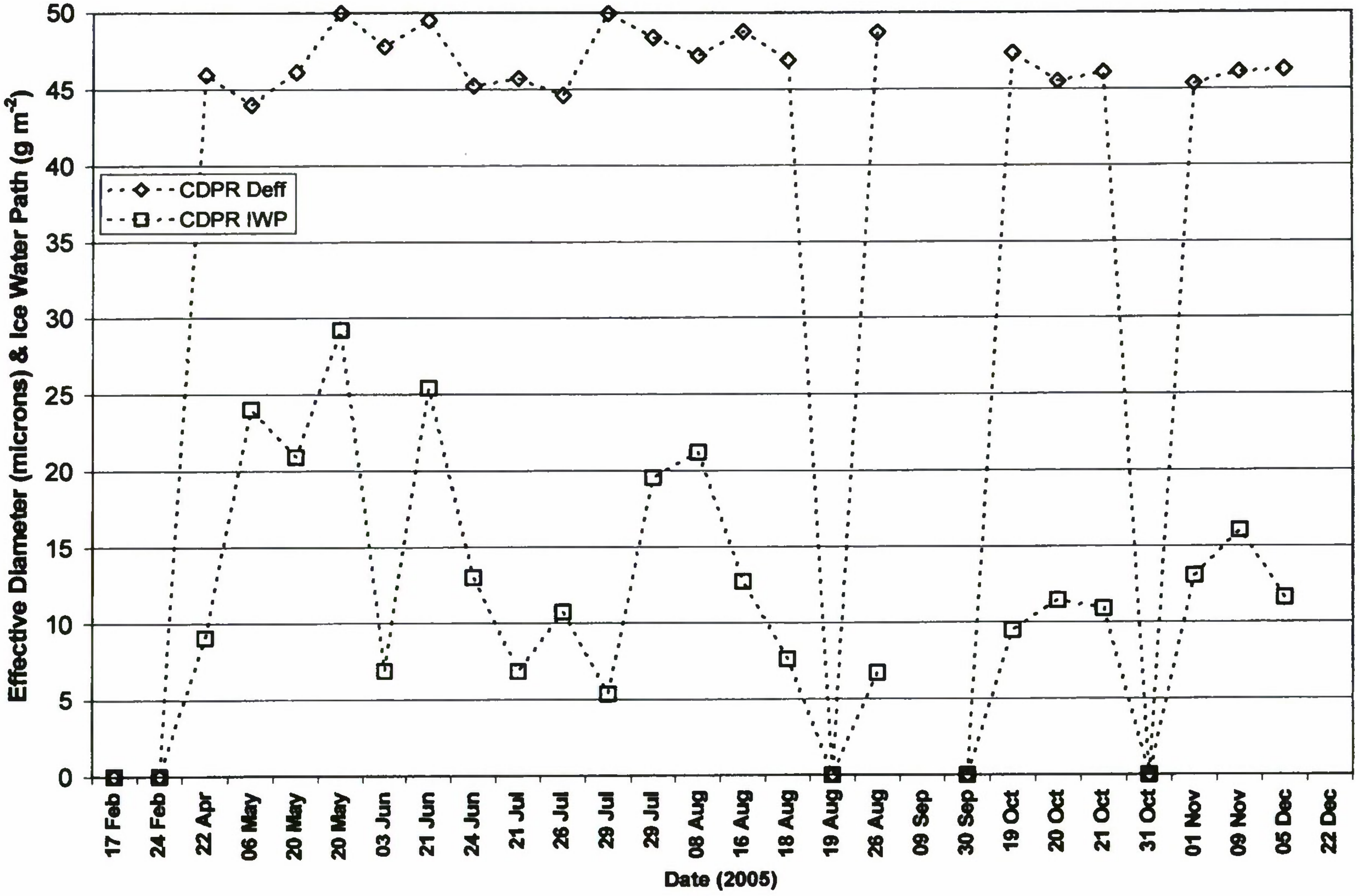

Figure 9. Effective diameter (µm) and ice water path (g mP^{-2P}) as retrieved by the CDPR algorithm for 26 observing periods.

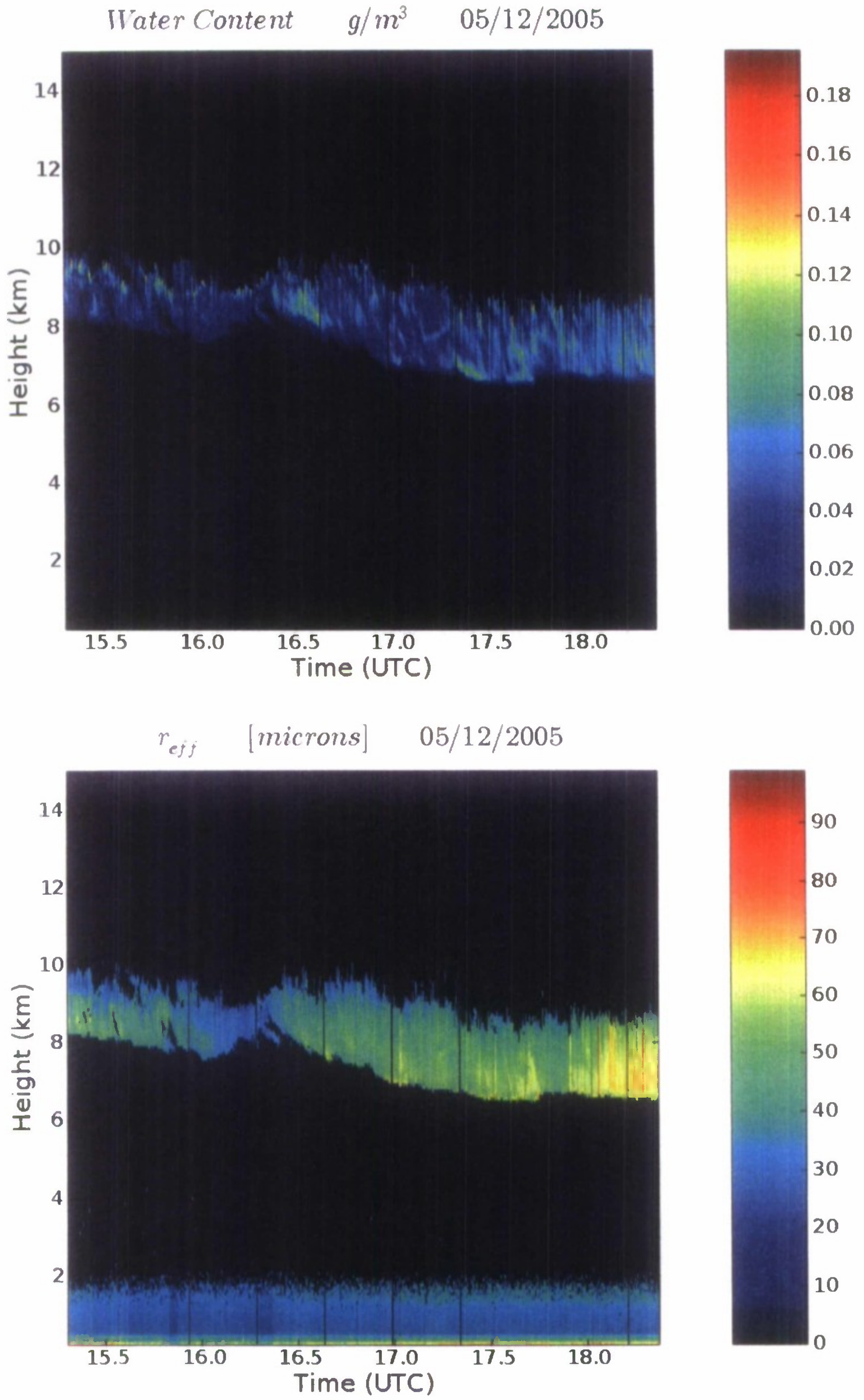

Figure 10. Radar/lidar IWC (upper) and rBeffB (lower) retrievals, 5 December 2005.

Table 3. A comparison of the retrieved values of rB_{effB} (converted to DB_{effB}, µm) and IWC (converted to IWP, g mP^{-2P}) from the radar/lidar cirrus measurements, with IWP and DB_{effB} retrievals from satellite imagery for observing periods in which significant amounts of liquid clouds were not detected by the lidar. Radar/lidar values represent the vertical and time average of all nonzero retrieved IWC, rB_{effB} values in the cirrus layer in the 10 minute period beginning at the satellite image time indicated.

Date/Time	CDPR D_{eff}	R/L r_{eff} X 2	CDPR IWP	R/L IWC X Δz
17 Feb/1545	0	58.78	0	16.41
22 Apr/1515	45.96	78.52	9.07	52.82
06 May/1145	44.01	76.14	24.04	70.19
20 May/1215	46.13	76.96	20.93	67.87
20 May/1415	49.98	95.24	29.21	122.20
21 Jun/1515	49.51	90.70	25.42	83.91
24 Jun/1415	45.23	59.00	12.99	26.51
26 Jul/1615	44.61	63.66	10.73	42.34
08 Aug/1315	47.20	83.82	21.22	83.06
31 Oct/1245	0	50.48	0	11.47
01 Nov/1915	45.35	56.24	13.05	22.55
09 Nov/1315	46.09	73.42	16.05	48.87
05 Dec/1615	46.26	62.98	11.60	37.08

First, it should be noted that the vertical extent of the cirrus layer as determined from nonzero retrieved IWC and rB_{effB} (e.g., Figure 10) is more limited than the layer depth and position as seen in the lidar backscatter and radar reflectivity (Figure 5). This is because the retrieval scheme requires both to be greater than the threshold for cirrus detection at a given time and altitude. For example, in Figure 5 lidar backscatter shows the layer top to be above 10 km until 1645, while radar reflectivity is greater than the detection threshold only up to 9 – 9.5 km so the retrievals are > 0 up to 9-9.5 km (see Figure 10). Both the top and the bottom of the layer drop to a lower altitude between 1645 and 1730 UTC, then remain relatively steady at that altitude. But after 1730 UTC, the radar signal extends to a higher altitude (> 10 km AGL) than the lidar signal due to an increasing IWC and thus more attenuation of the latter. This is very evident in a comparison of the original radar and lidar images (not shown) as used to determine radar and lidar base and top altitude as depicted in Figures 6 and 7. The top altitude for the IWC and rB_{effB} retrieval is again vertically constrained by the lower of the lidar and radar extent. So while the radar/lidar top altitude at 1615 UTC 5 December 2005 as shown in Figure 6 is 10.4 km AGL, the retrieval top is 9.2

km AGL. The Figures 6, 7 values use the higher top and lower base of the radar and lidar signals, while retrieval top and base represent the lower top and higher base of the two signals. This limitation can result in an underestimate of the vertical extent of the retrieved IWC and rB_{effB} from the radar/lidar measurements, either when greater ice concentrations near the cloud base attenuate the lidar or lesser ice mass near the cloud top are not detected by the radar.

Considering first the IWP values, it is immediately evident that the radar/lidar retrievals exceed the satellite retrievals in all cases, by an average factor of 3.4. Generally, the trend in the magnitude is similar from case to case. The smallest radar/lidar retrievals correspond to undetected (zero value) by the satellite and the largest values correspond as well. However, there are exceptions – for example, compare 24 Jun and 26 Jul. A comparison the DB_{effB} retrievals is consistent with the IWP comparisons – again, the radar/lidar estimates are consistently higher, here by about a factor of 1.6. Also, the temporal variation in the satellite DB_{effB} retrievals is much less, remaining very steady at a value of around 45 μm while radar/lidar DB_{effB} values vary between 50 and 95 μm. The magnitude differences offset each other in the computation of laser extinction. A larger IWP increases extinction, while a larger DB_{effB} decreases extinction. Thus, we expect a reduced difference in the computed extinction.

Because both sets of microphysical property estimates result from remote sensors and a sequence of approximations made to reduce the complexity of the retrieval algorithms, neither can be construed as a reference for the other. Instead, one can only consider the comparison as relative values. The retrievals from the active sensors may serve as a reference for the case-to-case variability of the satellite sensor retrievals.

5 LASER TRANSMISSION THROUGH CIRRUS LAYERS

As stated in Section 1, a major goal of this study was to show how laser transmission models applied to retrieved cirrus properties can be used to estimate the impact on transmitted power from an ADLS along the path through a cirrus cloud. In this section, we describe how cirrus properties estimated from the routine observing systems are used to specify the inputs to laser transmission models. Laser extinction from routine and reference observing systems are compared to demonstrate their relative potential effects on airborne laser systems.

Atmospheric transmittance (TB$_{s}$B) is the fraction of transmitted light (in units of power) that remains after the light has passed through a medium that in some way attenuates, or diminishes the light. If the transmitted power at its source is given by FB$_{0}$B, then the transmitted power at some distance *s* passing through an attenuating medium is

$$F_s = F_0 \exp(-\beta_e s)$$

where ßB$_{e}$ Bis the total extinction coefficient for the medium. The transmittance is the ratio of power incident at distance *s* to source power, so

$$T_s = \exp(-\beta_e s)\,.$$

In the case of laser light directed downward at an angle θ from the horizontal (called the scan angle) from a source at altitude *z*B$_{A}$B, the transmittance at a target of altitude *z* is desired. If the vertical distance *z*B$_{A}$ B- *z* is divided into layers of Δ*z* meters thickness, then the transmittance at the base of the *k*PthP layer from the source would be, in terms of the extinction coefficients for each layer,

$$T_{z_k} = \exp(-\frac{\Delta z}{\sin\theta}\sum_{j=1}^{k}\beta_{e_j})$$

where earth surface curvature is neglected.

The total extinction coefficient ßB$_{e}$B in a cloudy atmospheric layer is the sum of:

ßB$_{air}$B: molecular extinction coefficient of constituent gases
ßB$_{aer}$B: extinction coefficient of aerosols
ßB$_{cld}$B: extinction coefficient of cloud particles

all of which have units of mP^{-1}P. The optical thickness for the atmospheric layer is the product of the extinction coefficient and the layer thickness. So the slant path total optical depth of a cloudy atmospheric layer of depth Δz is

$$\tau = (\beta_{air} + \beta_{aer} + \beta_{cld})\frac{\Delta z}{\sin\theta}\,.$$

The atmospheric transmission code FASCODE (Clough et al., 1986) and the HITRAN molecular data base (Rothman et al., 1998) were used to compute the "clear-sky" optical depth in 20 m layers between a hypothetical laser source at 15 km AGL and the surface. This accounts for extinction due to air molecules (including water vapor absorption) and aerosol extinction. FASCODE was executed with a laser wavelength of 1.315 µm (from Ou et al., 2002) applied to the RAOB for each observational period. The absorption and scattering of light due to air molecules assumes a climatology of constituent gases that vary with altitude. For each computational layer, an integrated molecular concentration (molecules cmP^{-2P}) is computed by interpolation from climatological values that are a function of pressure and temperature as specified from the RAOB data. The total air molecular concentration for each layer is the sum of the integrated concentration of COB$_{2B}$, OB$_{3B}$, NB$_{2B}$O, CO, CHB$_{4B}$, OB$_{2B}$ and other trace gases. The RAOB relative humidity was used to determine the concentration of water vapor in each layer. The aerosol climatology is taken from the AFRL LOWTRAN (Kneizys et al., 1988) aerosol models – the "rural" model is used in this study. Its effect is primarily in the planetary boundary layer. Attenuation due to aerosols takes into consideration the effects of scattering and absorption of the laser light.

Three laser transmission models of extinction due to ice crystals were utilized only in the 20 m computational layers between the specified cirrus top and base altitudes. For the ice cloud layers, the extinction coefficient βB$_{cldB}$ was computed as a single value representing the mean value for the entire depth of the cloud. Mie theory (e.g, Bohren and Huffman, 1983), assuming spherical ice particles in a modified gamma size distribution, was used to provide one estimate of βB$_{cldB}$. Another estimate was provided using the parameterization of Fu (1996) in which 28 ice crystal size distributions from aircraft observations were used to provide empirical relationships for βB$_{cldB}$. These relationships account for the single scattering properties of hexagonal ice crystals. Both methods require the ice water content (IWC) and effective particle size (radius for Mie theory, diameter for the Fu parameterization) to be specified for the cloud layer. The bulk estimates of ice water path (IWP), cloud layer thickness (ΔzB$_{cldB}$) and effective diameter (DB$_{effB}$) as retrieved by the CDPR algorithm (Gustafson and d'Entremont, 2000) for the cirrus cloud layer detected from GOES-12 imagery were used to estimate IWC=IWP/ΔzB$_{cldB}$ and effective radius rB$_{effB}$= DB$_{effB}$/2 for the respective estimates of βB$_{cldB}$. These estimates were then applied at each 20 m computational layer deemed to reside within the ice cloud layer as diagnosed by the CMDF algorithm to represent the cloud layer's contribution to attenuation of the laser signal direct transmission.

The third laser transmission model for cirrus extinction was that of Ou et al. (2002), referred to as the UCLA model. While this model accounts for air molecule and aerosol extinction, these effects were disabled in the application of the model used here. The estimate of βB$_{cldB}$ from the Fu parameterization and the retrieved DB$_{effB}$ of the cirrus layer are inputs to the model, used to produce a βB$_{cldB}$ to compute direct signal power. The UCLA model computed signal power at the base of each cloudy computational layer due to direct transmission and forward scattering. The forward scattering was shown to often exceed 10% of the magnitude of the direct transmission. A laser beam of wavelength 1.315 μm, width 1.5 m, source power level (1 x 10P^{6P} W) and target diameter (3 m) were specified for the model calculations following Ou et al. (2002). The change in computed power between sequential computation layer bases from the UCLA model was converted to optical depth for the intervening layer.

The optical depth computed from the Mie, Fu and UCLA model methods for each cloudy computational layer was added to the FASCODE clear sky optical depth for the layer to determine the total computational layer optical depth (and thus the transmittance at the base of each layer) for each method. Summing the layer optical depths for all layers between the source and target altitude for a given source-target horizontal separation distance yielded the total optical depth along the laser path. The exponential of the negative of this total optical depth is the transmittance, or fraction of source power, present on the target. This calculation was made at each 20 m increment altitude between the surface and the source to yield a vertical profile of transmittance experienced on the target rising from a launch point at a specified horizontal separation distance from the laser source.

The laser transmission calculations using the Mie, Fu and UCLA models were first carried out using a small (10 m) horizontal separation distance to determine vertical optical depth and the maximum transmittance at any altitude. The UCLA model does not allow computation at zero separation distance. When 10 m is used, even if the laser source is as close as 3 km from the cloud top the scan angle at cloud top is 89.8°, or virtually vertical. This computation was made for all 21 cases for which cirrus microphysical quantities were retrieved by the CDPR algorithm. In two of the 21 observing periods, the vertical distance between the CDPR and CMDF cirrus top height estimates was greater than 2000 m. The temperature difference between the estimates was considered too great for the microphysical quantities from the CDPR algorithm to be representative of the CMDF cirrus top height. So these two cases were not included.

An example of the transmittance profile from the three cirrus laser transmission models and the clear sky transmittance is shown in Figure 11 based on the 1331 UTC 29 July 2005 RAOB. Also included is the direct transmission profile from the UCLA model. The laser source is at 15 km AGL and target is launched from 10 m horizontal separation distance and rises to the source altitude. The clear sky profile is based on FASCODE optical depth in 20 m layers from source altitude to surface. The Mie, Fu and UCLA (direct power and total power = direct + forward scattered power) laser transmission models are applied to compute cloud optical depth in each 20 m layer within the cirrus deck, in this case between 9.87 and 11.71 km altitude. Total optical depth is used in each 20 m layer between source and ground to compute transmittance at the base of each layer. Comparing transmittance profiles, it is clear that the cirrus attenuation is much greater than the clear sky attenuation. For the vertical laser path, the transmittance is very nearly invariant with height above and below the cloud layer, with a steep transmittance gradient present in the cloud layers for the ice cloud transmission models. In this case, the cirrus optical depth for the UCLA direct transmission was 0.55 and for total (direct + forward scattered) was 0.48. This represents a 7% increase in transmission through the cloud layer when forward scattered power is included.

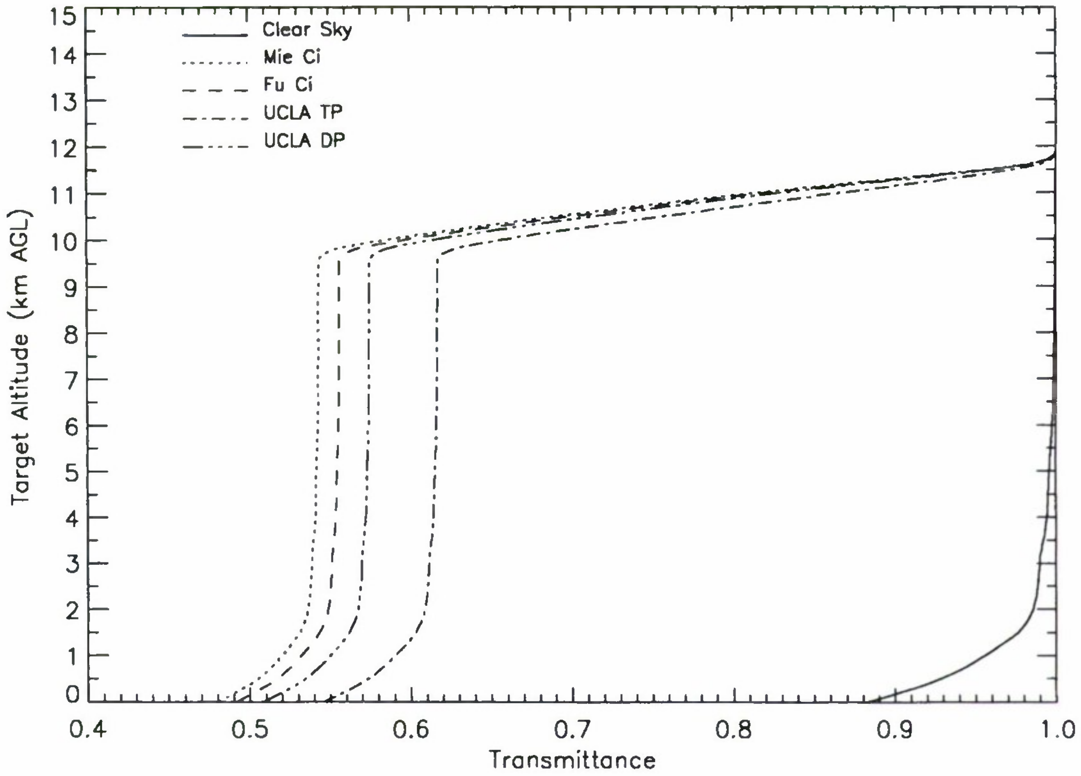

Figure 11. Target transmittance profiles for the 1331 UTC 29 July 2005 RAOB sounding, CMDF cirrus top and base height, and CDPR microphysical retrievals.

The laser transmission computations were then carried out on the data from the 1331 UTC 29 July 2005 case using 5 km increments of horizontal separation distance (Δx) from 5 to 100 km. The atmospheric conditions (both atmospheric state profile and cirrus properties) are assumed to be invariant in the horizontal. This allows the determination of the impact of altitude and separation distance on the transmission for real conditions as measured in a single location. Results from the $\Delta x = 50$ km case are shown in Figure 12.

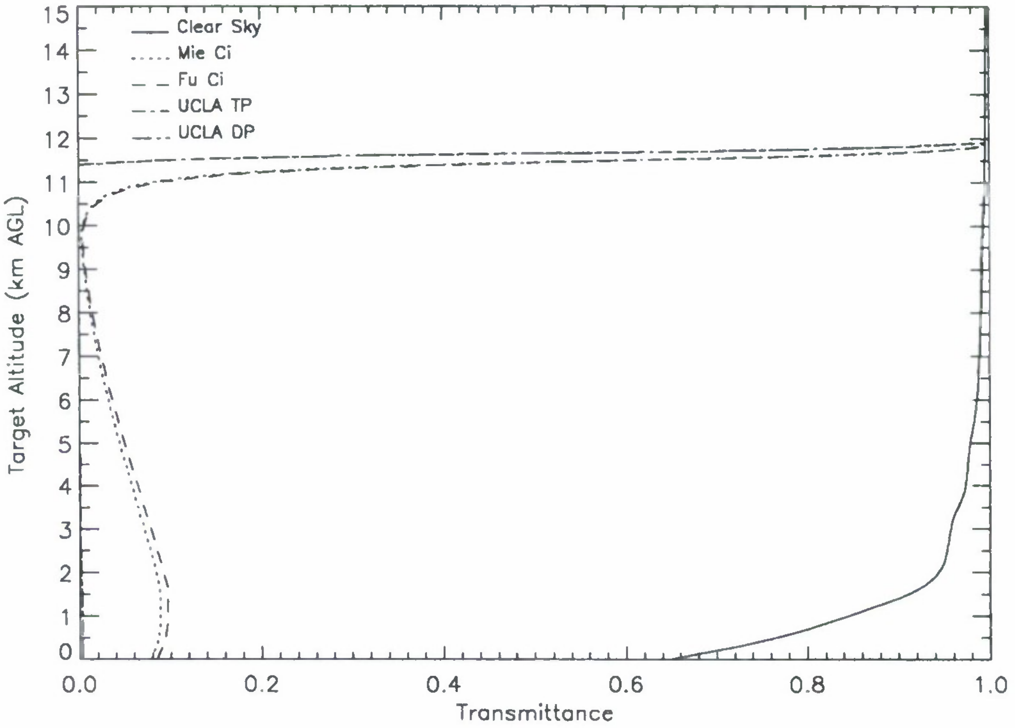

Figure 12. Same as in Figure 11 except target is launched at a horizontal separation distance of 50 km from the laser source.

In comparing Figures 11 and 12, several differences are apparent. First, the transmittance gradient through the cirrus layer is greater for $\Delta x = 50$ km in all three transmission models. Second, the difference between Mie and Fu models and between UCLA direct and total power results are greatly reduced, with the latter being essentially zero at all levels. This suggests that forward scattering makes virtually no additional contribution to the total power at smaller scan angles, which is expected. Third, the transmittance for altitudes below the cirrus layer increases with decreasing altitude down to the top of the boundary layer (where aerosol concentrations are greater) for all three models. This is also to be expected, since scan angle increases with decreasing target altitude, thus the laser path length through the cloud layer is shorter resulting in less attenuation.

Figure 13 depicts cirrus vertical optical depth at 1.315 µm for the 19 cases as computed by the laser transmission models as applied to the DB_{effB}, IWP and ΔzB_{cldB} retrieved by the CDPR algorithm and the geometric cloud depth as determined by the CMDF algorithm. The latter was included in the plot because of its contribution to cloud optical depth. The other factor is the model-dependent extinction coefficient βB_{cldB}. This in turn depends on the satellite retrieved D_{effB} and IWP. The difference in optical depth among the models is relatively small compared to their differences between observation cases. For optical depths less than 1.5, there is a tendency for the UCLA values to be less than the Mie and Fu values, whereas the reverse is generally true for greater optical depths. Note that there is not necessarily a correlation between optical and geometric depth. For example, in the period 8-18 August, the optical depths decrease while the geometric depths increase. Looking back to Figure 9, we see that the IWP also decreases during this period while the effective particle sizes remain relatively constant. From this we see that cirrus optical depth as derived from the routine observations is primarily determined by the $IWC=IWP/\Delta z_{cldB}$ from the satellite imagery and geometric depth from the RAOB profile.

In the discussion above, we noted how changes in horizontal separation distance, which changes the path length for a given target altitude, affects the transmittance profile. The results of this analysis for Δx at 5 km intervals from 5 to 100 km (and at 10 m as depicted as $\Delta x = 0$) are shown in Figure 14 based on the routine cirrus retrievals. As seen in Figures 11 and 12, the Mie and Fu transmittance profiles are more similar to each other than to the UCLA profiles for non-zero separation distances. This is partly due to the forward scattering explicitly computed in UCLA model, especially at short separation distances. What stands out in the cirrus transmittance plots in Figure 14 is the fact that, especially beyond $\Delta x = 10$ km, the transmittance contours ≥ 0.5 are essentially invariant with separation distance. This suggests that the laser scan angle is inconsequential in the degree of penetration of the laser signal when it is less than about 20°, regardless of the laser model. For greater scan angles, the transmission through the cirrus layer is greater, but the horizontal separation distances are unrealistically small compared to what are expected to occur in actual engagement scenarios.

It is of interest to compare the degree of effect on laser transmittance of the cirrus microphysical properties as retrieved from the radar/lidar

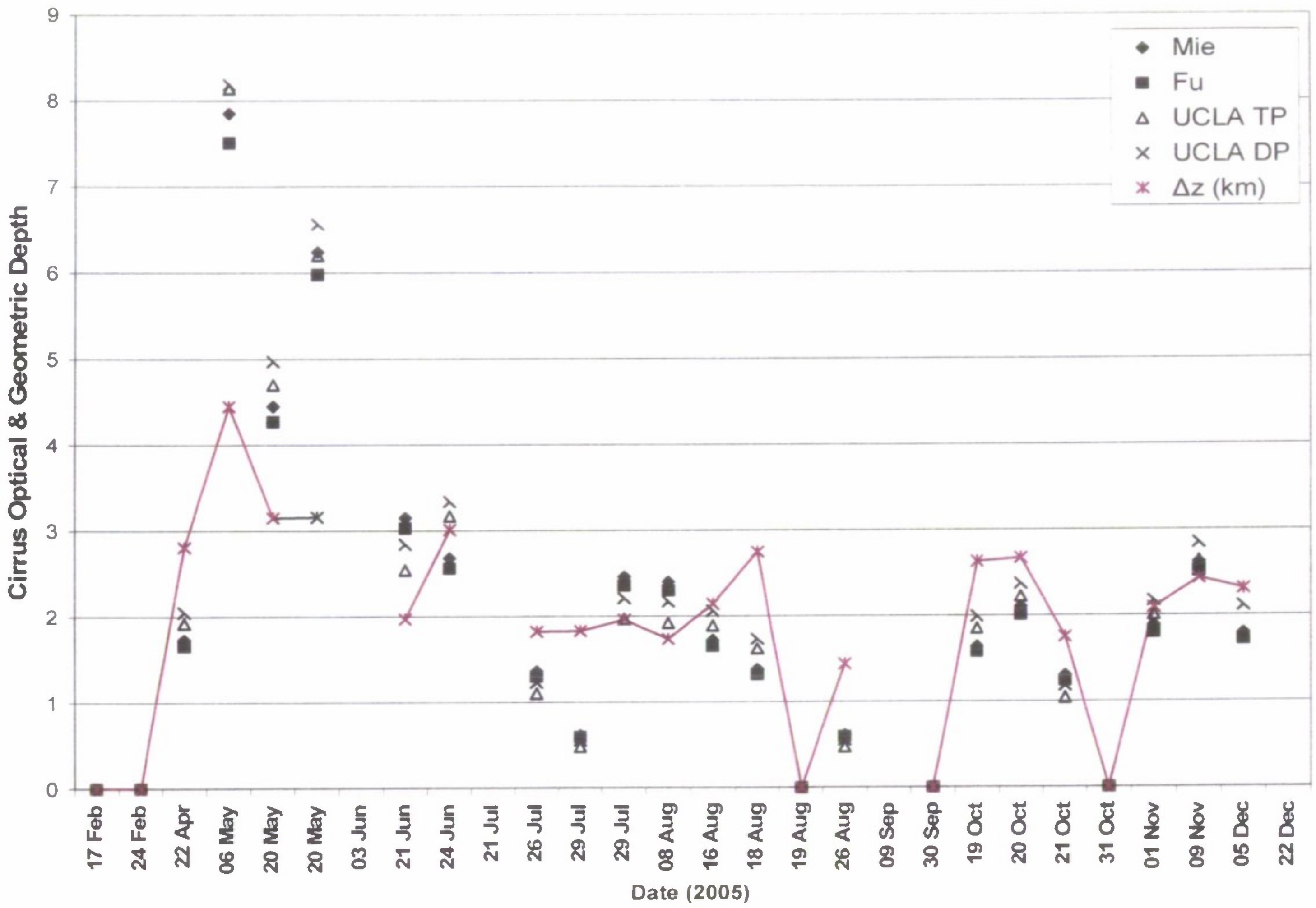

Figure 13. Cirrus optical depth as computed from the laser transmission models applied to CDPR microphysical property retrievals, and CMDF geometric cirrus depth.

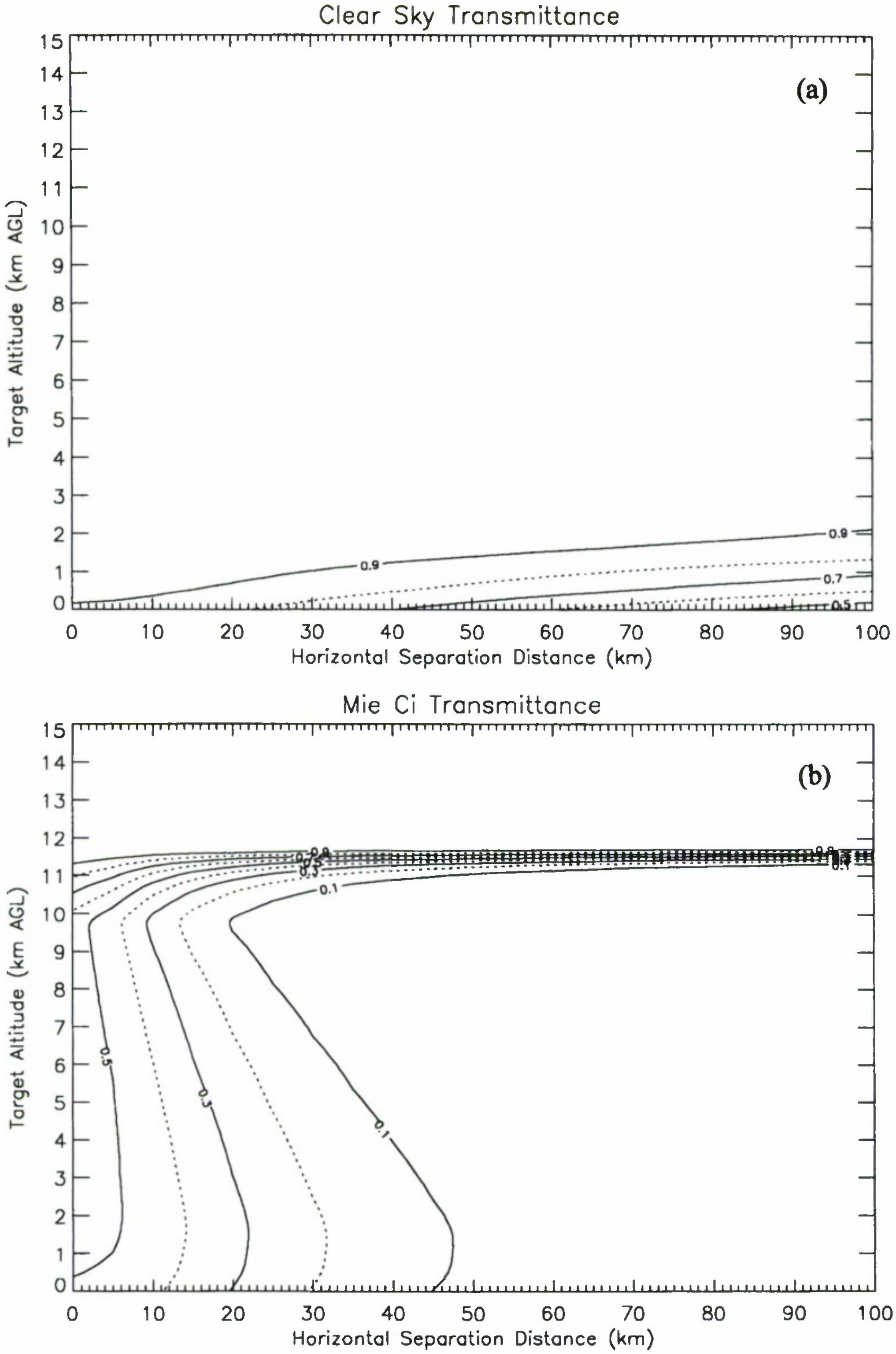

Figure 14. Target transmittance as a function of target altitude and source-target horizontal separation distance for a source at 15 km AGL for (a) clear sky and (b) Mie cirrus model. Case shown is same as in Figures 11 and 12 using same microphysics, geometric retrievals.

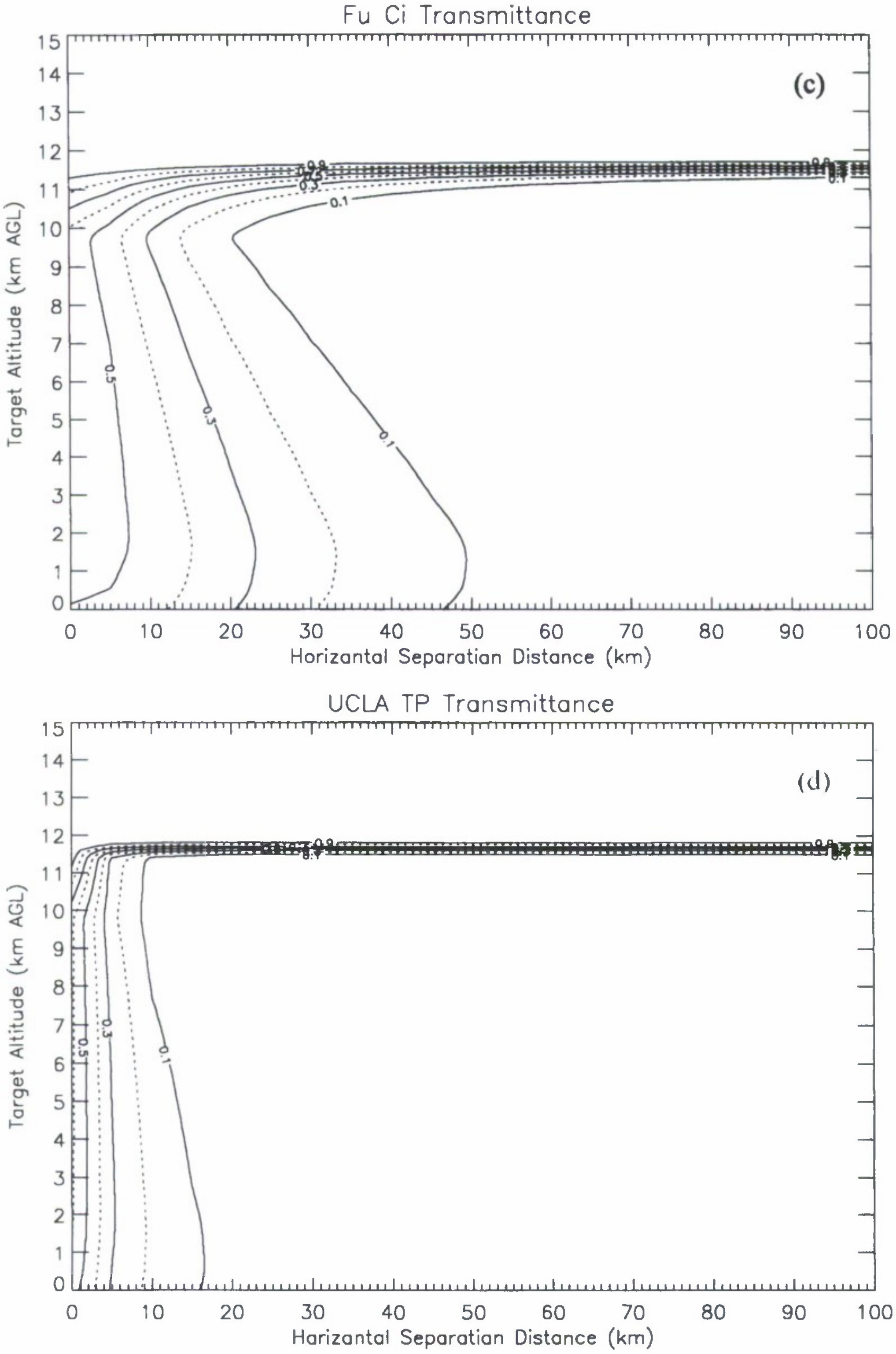

Figure 14 (cont.). Target transmittance as a function of target altitude and source-target horizontal separation distance for a source at 15 km AGL for (c) Fu and (d) UCLA total power cirrus models.

measurements with those retrieved from the satellite imagery. As stated in Section 4.3, the requirement for both radar and lidar cirrus signal constrains the retrieved properties to a vertical extent that may be less than the actual cirrus thickness. Therefore, it is fitting to compare the transmittance effects in light of the differences in bulk extinction and geometric thickness to account for the relative contributions of each in the bulk optical depth of the cirrus layer.

In Figure 15, we show the bulk extinction coefficient (from the Fu, 1996 model) computed from the satellite- and R/L-retrieved particle size and ice water content for the cases included in Table 3. We have plotted them against the retrieved cirrus layer thickness (top height – base height) for R/L, and the thickness as determined from the RAOB-based CMDF diagnosis to represent the satellite retrieval. For reference, lines of constant vertical optical depth (tau) are included in the figure. There is a tendency for the R/L thicknesses to be of lesser magnitude, consistent with the underestimation of the vertical extent as mentioned above. But the extinction values derived from the R/L particle size and ice water content retrievals are generally larger than those derived from the satellite retrievals. The product of the extinction and the cirrus thickness is the bulk optical depth, which as the figure shows are mostly in the same range for the CDPR and R/L. Thus, the lesser geometric thickness in the R/L retrievals is compensated by the greater laser extinction in the overall determination of transmittance. While the R/L retrievals produced a smaller geometric thickness and the satellite retrievals resulted in a lesser value of laser extinction, the optical depth derived from the two observing systems are generally comparable.

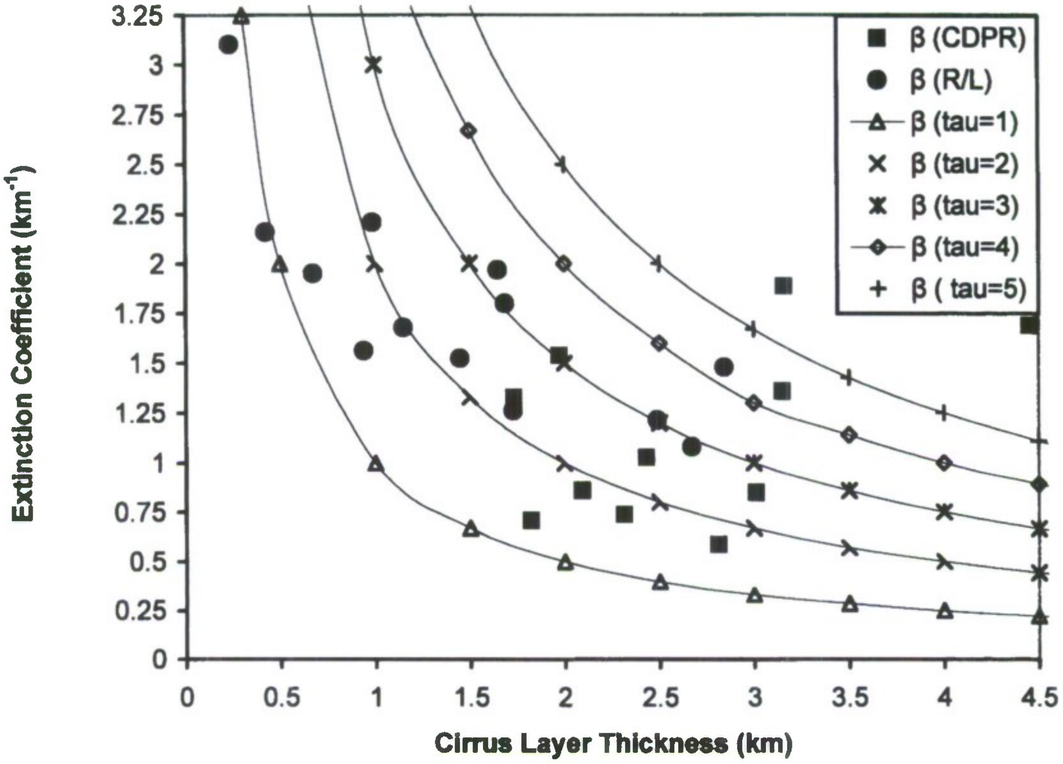

Figure 15. Extinction coefficient (Fu, 1996) vs. cirrus thickness for the non-liquid cloud cases shown in Table 3 (11 for CDPR, 13 for R/L). Lines of constant optical depth (tau) are shown for reference. Thickness for CDPR are actually taken from the RAOB-based CMDF diagnosis of cirrus top and base altitude. Note that the two R/L points with tau < 1 are for the cases in which the CDPR failed to detect cirrus.

6 DISCUSSION

The primary purpose of this project was to determine if routine cirrus observations could lead to reliable estimates of cirrus impact on the operation of an Airborne Defensive Laser System. To accomplish this, it was necessary to derive the relevant geometric and microphysical properties of cirrus across a range of conditions. While the required properties could best be measured by means of an airborne optical array probe flown through the cirrus, such instrumentation was not available due to funding limitations. This project was limited to the use of ground-based active remote sensors as they were available at their home location to avoid the expense of their relocation. In addition, manpower availability was limited to week days during regular business hours to avoid the requirement of additional work details.

With these restrictions, and with a supply of some 30 Vaisala RS92-SGP radiosondes, the field experiment began in February 2005 and required approximately 11 months to find enough suitable cases to use the 30 sondes (one failed and one was used for another project, leaving 28 for the cirrus experiment). A radiosonde was released no sooner than 30 minutes after the start of a three-hour observing period conducted with the AFCPR 35 GHz radar and PEELS 1.574 µm lidar. Lidar is subject to specular reflection when pointing at zenith. Therefore, the radar and lidar were co-pointed at a fixed elevation of 85°. An observing period was declared if our forecast predicted a high likelihood of at least three hours of cirrus overhead, with not more than scattered lower clouds at any time during the period. Twenty-six such observing periods were documented in the 11-month field experiment, during which 28 radiosonde observations (RAOBs) and simultaneous surface observations were taken in the minimum three-hour period of operation of the radar and lidar. GOES-12 satellite imagery at 30-minute intervals was collected and analyzed in the 26 observing periods as well. The imagery time at or just after the sonde launch served to provide the cirrus microphysical retrievals used in conjunction with the cloud layer base and top altitude derived from the RAOB to represent the "routine" observations' specification of the required cirrus properties. The same quantities retrieved from and measured by the radar reflectivity and lidar backscatter power represented the required cirrus properties from the "reference" sources.

A reliable determination of the cloud vertical structure (CVS) was obtained from the reference measurements of the radar and lidar. Extraction of the base and top altitudes of the cloud layers from printed images of the reflectivity and backscatter respectively led to estimation of the base and top to within about 200 m. The uncertainty stems from an unknown sensitivity of the lidar to very low ice crystal concentration on cloud edges, the degree of precision of the printed images and the correction of the extraction times to account for the RAOB drift. The latter was taken into account in order to permit the comparison of top and base altitudes between the radar/lidar (R/L) specification and the radiosonde-inferred values. These were determined using an empirical algorithm that relies upon statistical best fit of relative humidity with respect to ice saturation (RHB_{iceB}) and cloud/no cloud as determined by simultaneous R/L measurements. The algorithm coefficients had been developed on previous field experiment data using RS80 radiosondes. The algorithm was applied to the RS92 RAOBs in the current project to diagnose cloud probability (CP) at each report level. The diagnosed tops of cirrus were restricted to be at or below the tropopause as determined from the RAOB. The empirical algorithm is part of the Cloud – Meteorological Data Fusion (CMDF) which also incorporates the retrieval of cirrus top from the satellite imagery and the surface observation of cloud base to augment the RHB_{iceB} determination of the cirrus top and base altitude in case the empirical scheme fails to detect a cloud layer. In fact there were no cases where the empirical scheme failed to detect the observed cirrus layer in the 28 RAOBs analyzed in this project.

Cirrus microphysical properties were retrieved from the satellite imagery with the aid of numerical weather model gridded profiles of temperature, pressure and geopotential height. The properties of interest in this project were cloud top height, effective particle size and ice water path. The cloud base height was also used to convert ice water path to layer average ice water content. An independent retrieval of effective particle size and ice water content was conducted using the co-pointing radar reflectivity and lidar backscatter for selected cases as a demonstration of a newly-acquired retrieval scheme.

Cloud vertical structure as diagnosed from the CMDF algorithm applied to the RAOBs and from the satellite retrieval was compared to the reference R/L measurements. The cirrus top altitude from the R/L measurements was found to vary much more than the tropopause height among the observation cases. Fully 25% of the observing periods had cirrus tops significantly lower than the tropopause. When the tropopause height assignment was near the measured cirrus top, there was an uncertainty as to which was higher. In most of the cases in which the R/L cirrus top was higher, it was within the 200 m R/L measurement uncertainty of tropopause. The empirical RH – CP algorithm diagnosed cirrus tops that showed the same degree of temporal variation as the R/L specifications. In contrast, the cirrus tops retrieved from the satellite imagery did not demonstrate the degree of temporal variation, and in five cases failed to detect cirrus in the celestial dome above the surface observer. While no attempt was made in this project to determine the false alarm rate in the CMDF-detected cirrus, its perfect probability of detection indicates that there is a capacity for identifying cirrus layers not detected from the satellite analysis. This suggests the benefit of using sensitive radiosondes in conjunction with satellite imagery to support live tests of ADLSs in the absence of a ground-based lidar to ascertain the possible presence of cirrus. However, more work needs to be done to determine whether or not the CMDF algorithm may result in false alarms, indicating the presence of cirrus when in fact it does not exist.

The satellite retrieval of cirrus top height was systematically lower than the R/L measurement. In fact, the negative bias of the satellite estimate was about 3.7 times that of the CMDF algorithm, averaging more than 1 km below the R/L top height. This is in part due to the fact that the radiation emitted from the cloud layer is primarily from a level below that of the upper cloud edge where the ice crystal concentration is greater. Relying on the satellite estimate of cirrus top height may prove overly optimistic in terms of ADLS operation. Supplementing with a sensitive radiosonde would tend to reduce the cirrus top position error estimate, according to the results of the current study.

When the tropopause restriction was removed, the CMDF algorithm bias changed from a moderate negative bias to a greater positive bias. This apparent overestimate of the cirrus top altitude was not reduced when the coefficients derived from RS92 soundings were used in the empirical scheme. This suggests that greater accuracy in determining cirrus top height may require a tuning of the CMDF algorithm to reduce the overestimate of the top altitude of the cirrus.

The CMDF algorithm performed remarkably well in diagnosing the base altitude of cirrus clouds. Its accuracy was determined to be at the level of uncertainty of the R/L measurements. Though the comparisons with R/L base heights indicate a small positive bias, it is uncertain if there is indeed a systematic error in the CMDF base height diagnosis because of the level of R/L uncertainty. What this performance does indicate is that the CMDF algorithm applied to a radiosonde sensitive to water vapor variations in the upper troposphere can be a reliable way to measure cirrus base heights. This may have implications for deployment of an ALDS intended to operate at lower altitudes.

In this study, the satellite retrieval imposed a default thickness for the cirrus layer. This resulted in a cirrus layer depth that averaged about four times less thick than the CMDF-diagnosed thickness (estimated to be about 0.5 km thinner on average than the depth from the R/L measurements). Because of this limitation of the satellite retrieval of the geometric cirrus properties, the height of top and base from the CMDF algorithm was used along with satellite imagery-retrieved microphysical properties in the laser transmission computations.

The cirrus coverage as determined from the satellite imagery was compared with the surface observation at the time of RAOB launch. Results showed a tendency of the satellite cloud mask to under-detect the coverage of cirrus, especially when the long-wave emissivity of the cirrus was low. No attempt was made to diagnose cirrus cloud coverage from the RAOB data in this project. So the use of a surface observer, especially when no lower clouds are present, is an important supplement to the use of satellite imagery in supporting an ADLS test operation.

The bulk effective particle size and ice water content as retrieved from the satellite imagery and from the radar reflectivity and lidar backscatter were compared for observing periods in which a minimal amount of liquid cloud was present. Though both result from retrieval techniques that employ simplifying assumptions, the values from active sensors were thought to be more representative of the cirrus vertical profile than those from the passive satellite sensors. This is because the active sensors are getting returns at intervals through most of the cirrus layer, while radiance sensed by the satellite originates mostly from near the cirrus top. Effective particle diameter from the satellite imagery showed very little temporal variation, considerably less than the variation of the ice water path. By contrast, the cirrus layer mean particle size retrieved from the R/L measurements varied significantly with cirrus event. For the cases we analyzed, the retrievals of IWP inferred from the radar/lidar measurements were on average more than twice the corresponding satellite retrievals. The effective particle radius retrievals were also significantly larger than the satellite-retrieval values. This is to be expected in a satellite-based bulk retrieval since usually the smallest particles are nearest the top where the temperatures are lowest. The ground-based remote sensors are generally both going to get returns from the lowest portions of the cirrus clouds where particle sizes are the largest.

Three different cirrus extinction models were applied to the geometric and microphysical retrievals to determine the transmittance, or fraction of originating laser power, in a profile between the source (nominally set at 15 km altitude) and a hypothetical target rising from the ground to the source altitude. Transmittance through an atmospheric layer is simply the exponential of the negative of optical depth of the layer. The cirrus optical depth is a product of the extinction coefficient and the geometric depth of the cirrus layer. The extinction coefficient, determined by each laser transmission model, is dependent on the retrieved particle size and ice water content. In the satellite sensor retrievals, only two of the 28 cases resulted in cirrus optical depths (at a laser wavelength of 1.315 μm) of less than one. This is due to the fact that the cirrus was sometimes undetected by the satellite algorithm in cases of optical depth less than one. The clear sky optical depth was also computed, but its effect on laser power is minor compared to cirrus optical depth. The difference in computed cirrus optical depth among the three models was small compared to the temporal variation among observing periods.

Cirrus properties retrieved from satellite imagery for an individual case (that had a vertical optical depth of about 0.5) were used as input to the laser transmission models executed in a sequence of computations. The horizontal range between the laser source and target varied between zero and 100 km in the model runs. The results showed that, beyond a horizontal separation distance of about 10 km (indicating laser angles of less than 20°), the transmittance values above 0.5 were essentially invariant with separation distance. Laser attenuation due to transmission through the cirrus layer was much greater than clear sky attenuation. This makes it important that the presence of cirrus and its altitude in the region of interest is known before an ADLS is deployed for tests or operational missions.

The larger particle sizes and larger ice water content R/L retrievals had counteractive effects on the laser extinction, with the larger IWC making for larger extinction and the larger particle sizes influencing a smaller extinction. Still, a comparison of the cirrus extinctions at laser wavelengths showed that those derived from the R/L retrievals were generally larger than those derived from satellite retrievals. However, the requirement that both lidar and radar detect cirrus at a location and time resulted in microphysical retrievals that were more limited in vertical extent than the actual cloud layer. This was due to lack of radar sensitivity when the cloud mass was low and lidar attenuation when the cloud mass was great. The greater extinction of the R/L retrievals combined with the greater geometric thickness of the cirrus used in the satellite computations led to comparable values of the total cirrus optical depth. However, without an independent reference measurement of the cirrus microphysics in this project, no definitive conclusion on the adequacy of the retrieved microphysical properties can be drawn.

These results suggest that, with the current algorithms, satellite detection and property assignment alone cannot satisfy the requirements of determining the necessary characteristics of cirrus for ADLS deployment. The satellite detection algorithms miss the thinnest cirrus cases that can be detected by a surface observer, and even with a sensitive radiosonde. Fictitious diagnosis of cirrus from a RAOB when a moisture maximum occurs in the $\mathrm{RHB}_{\mathrm{iceB}}$ profile can't be ruled out. But the perfect probability of detection in the radiosonde profiles seen here suggests that a lack of such a moisture maximum would prove the non-existence of cirrus to virtual certainty. The current satellite algorithm tends to underestimate cirrus top height by at least a kilometer on average, which could be remedied largely through the use of a radiosonde sensitive to water vapor variations in the upper troposphere.

Because cirrus clouds appear to have a potential power-reducing effect on the laser beam, their horizontal and vertical position should be known accurately. The results of this study suggest that a suitable radiosonde observation may be a satisfactory alternative to ground-based active remote sensors for determining the existence and vertical position of cirrus in support of an ADLS test or deployment. Laser transmittance estimates in a region covered by cirrus based on satellite retrievals would result in realistic spatial variations, but their absolute reliability would be uncertain. There is a need to compare both satellite-based and active sensor-based ice cloud property retrievals with ice microphysical measurements in order to more definitively determine their accuracy. Ongoing cirrus characterization studies should shed more light on the reliability of ice particle mass and size retrievals from active and passive remote sensors.

APPENDIX A.

ACCOUNTING FOR RAOB DRIFT IN RADAR/LIDAR CLOUD MEASUREMENTS

The purpose of this appendix is to describe a technique to estimate the time when a vertically pointing radar or lidar observes a cloud segment through which a rawinsonde observation (RAOB) is taken after launch from the same ground site. This technique attempts to account for the downwind drift of the RAOB from the time of its launch to the time it reaches cloud base altitude. To describe the technique, we use a time-height cross section of cloud observations by a vertically pointing TPQ-11 35 GHz radar at Hanscom AFB, MA on 14 June 2002 (not shown).

The first step is to compute the downwind displacement of the sonde during the time period of ascent Δt_a from time of launch tB_{lB} until the time tB_{cB} it reaches cloud base altitude. "Downwind" is in reference to the wind direction at the cloud base level, since once a cloud segment is observed by the radar/lidar, we assume it is advected in this direction. To estimate Δt_a for this computation, we find the elapsed time at which the RAOB first reports a height ≥ the height zB_{lB} of the cloud base observed by the radar or lidar at tB_{lB}. The following data segment is taken from the RAOB launched at 1210 UTC on 14 June 2003.

t	p	z	T	RH	s	d
1290	424.20	6960	255.2	45	24.8	263
1292	423.90	6965	255.1	45	-99.9	-99
1294	423.60	6971	255.1	45	-99.9	-99
1296	422.80	6985	255.0	45	-99.9	-99
1298	422.30	6994	254.9	45	-99.9	-99
1300	421.70	7004	254.8	46	24.8	262
1302	420.60	7024	254.6	47	-99.9	-99
1304	420.10	7033	254.5	48	-99.9	-99
1306	419.70	7040	254.4	49	24.7	261

The elapse time from launch is given in the column marked "t" in seconds and the sonde's altitude is in the column marked "z" in meters. At time tB_{lB}, $zB_{lB} = 7.0$ km, so from the RAOB data we estimate Δt_a at 1300 seconds or ~ 22 minutes. This means that the time tB_{cB} at which the sonde reaches cloud base is $t_c = t_l + \Delta t_a$ or ~ 1232 UTC. The downwind displacement DBsB of the sonde from the ground site can then be estimated from the product of the average wind speed $\bar{s}$ in the downwind (at cloud base level) direction during the ascent period and the ground-to-cloud base ascent duration Δt_a. The average downwind wind speed can be computed from $\bar{s} = \frac{1}{\Delta t_N}\sum_{i=1}^{N} s_i \cos(d_i - d_c)\Delta t_i$ where N levels of wind data are available between the surface and zBlB at time intervals Δt_i, Δt_N is the time between launch and the *N*th wind level and dBcB is the wind direction of that level. So an estimate of downwind displacement is computed from $D_s = \bar{s}\cdot\Delta t_a$. Using the RAOB data from this case, dBcB = 262° so that $\bar{s}$ = 7.8 msP^{-1}P and DBsB = 10.2 km.

At the time tBcB the sonde reaches cloud altitude, it encounters a cloud segment that had been observed by the radar/lidar $\Delta t_{r/l}$ earlier than tBcB. This is the amount of time required for the cloud segment to move from over the ground site to the location downwind where the sonde encounters the cloud. This distance is the downwind displacement DBsB so $\Delta t_{r/l} = \frac{D_s}{s_c} = \frac{\bar{s}\cdot\Delta t_a}{s_c}$ where sBcB is the wind speed at cloud base altitude zBlB. Then the time of observation of that cloud segment by the vertically pointing radar/lidar is $t_{obs} = t_c - \Delta t_{r/l}$. Because sBcB is usually larger than $\bar{s}$, $\Delta t_{r/l}$ is usually less than Δt_a so tBobsB will be after tBlB but before tBcB. In this case, sBcB = 24.8 msP^{-1}P so $\Delta t_{r/l}$ = 7 minutes and tBobsB is 1225 UTC. This is the time at which we should use the height of the cloud base zBobsB as observed by the radar/lidar, which for this case is ~7.2 km.

The same computation should be made for the time at which to use the cloud top height as well. In this case, zBlB = 11.7 km, Δt_a= 37 minutes so tBcB = 1247 UTC, dBcB = 272°, $\bar{s}$ = 19.9 msP^{-1}P and DBsB = 44.1 km, sBcB = 50.5 msP^{-1}P so $\Delta t_{r/l}$ = 15 minutes and tBobsB is 1232 UTC. At this time, the cloud top height is observed by the radar as ~ 11.8 km.

Note that if digitized radar/lidar data were used to determine cloud base and top altitudes instead of subjectively from the radar time-height cross section, data files from the radar/lidar and RAOB would be the only inputs necessary to perform an automated computation of the cloud base and top altitude to compare with the RAOB humidity data.

Several simplifying assumptions are made in designing this technique. First, in computing a correction for ascent-average wind speed to account for directional wind changes, crosswind (at cloud height) variation of the cloud height is neglected. If directional changes are present, the sonde will lie off the line marking the cloud height wind direction when it achieves this altitude. So it would actually be encountering a cloud element that moved parallel to the element earlier measured by the radar/lidar. Second, it is assumed that cloud base/top height remains constant during the period $\Delta t_{r/l}$ as it is advected by the wind at cloud base height. Thirdly, the difference between ascent-average wind speed and cloud base/top wind speed is neglected in estimating Δt_a by using zB_{IB} for this estimate. This is difficult to avoid because one must start with some initial specification of the cloud base height. Perhaps one could get a more “fine tuned” estimate of tB_{obsB} by using the resulting zB_{obsB} as zB_{IB} and repeating the computation process. Considering the other assumptions, this seems unnecessary.

APPENDIX B.

AN EMPIRICAL METHOD TO DEDUCE CLOUD PROBABILITY IN A RADIOSONDE SOUNDING

Radiosonde observations (RAOBs) provide accurate soundings of pressure, temperature, humidity and winds for characterization of the atmospheric state. However, they do not make explicit measurements of cloud properties. An empirical algorithm was devised to take advantage of the high precision in-situ data from RAOBs in estimating the vertical boundaries of cloud layers. The algorithm is based on the association between maxima of relative humidity and the presence of cloud layers. Relationships between cloud probability and relative humidity CP=f(RH) were developed that could be applied to sounding data to determine CP at each level.

A series of 19 RAOBs taken in varying cloud conditions and accompanied by co-pointing radar and lidar constituted the development data for the algorithm. The soundings were taken at Hanscom Air Force Base, MA on various dates in July and August 2001 and June – August 2002. The 35 GHz Air Force Cloud Profiling Radar (AFCPR) and the 1.574 µm Portable Electronic Eyesafe Laser System (PEELS) measured reflectivity and backscattered power continuously during the RAOB flights. The AFCPR and PEELS time-height cross-sections were used to determine the base and top altitude of each observed cloud layer. The higher of the radar or lidar top and the lower of the radar or lidar base was used in each case. In several of the soundings multiple cloud layers were present.

Relative humidity with respect to ice saturation (RHB_{iB}) was computed at each sounding level in which $T < 0$ C from measured P, T and RH. Relative humidity used in developing the relationships for CP was set to measured RH (RHB_{lB}, assuming saturation vapor pressure with respect to a liquid surface) at levels where $T \geq 0$ C, computed RHB_{iB} where $T \leq -40$ C, and a temperature-weighted average of RHB_{lB} and RHB_{iB} where $0 \text{ C} > T > -40$ C ($RH = w \times \mathrm{RHB}_{lB} + (1-w) \times \mathrm{RHB}_{iB}$, $w = T/40+1$). Then separate relationships of the form $CP = (a0 \times a1P^{RHP} + a2)P^{-1P}$ were created for each temperature regime using a curve fitting algorithm in the process described next.

Each sounding and the corresponding radar/lidar measurements of cloud top altitude (CTA) and cloud base altitude (CBA) are matched. We selected the measured CBA and CTA at the estimated times when a vertically pointing radar or lidar observes a cloud segment through which the sonde enters and exits after launch from the same ground site. This technique attempts to account for the downwind drift of the sonde from the time of its launch to the times it reaches cloud base and top altitude. CBA and CTA estimates are then "fine tuned" by comparing them with the development RH values to place them where abrupt changes in the sounding are apparent near the estimated CBA and CTA levels. A value of CP=1 is set for all sonde report levels lying between or at CBA and CTA for all cloud layers observed by the radar/lidar, and CP=0 elsewhere.

All of the development RH and CP pairs at all levels in all of the soundings are binned by temperature regime, except for those levels within 500 m of the ground or above the tropopause (unless CP=1 for the latter case) as determined by the algorithm of Roe and Jasperson (1980). For each temperature regime, the total number of report levels are counted (NRHT) for each integer value of development RH (0-100%), and the number of report levels with CP=1 are also counted (NRHC) for each 1% RH bin. Then for each development 1% RH bin, the probability of cloud occurring for that RH is CP_Ratio = NRHC/NRHT. A five-pointed weighted running mean (CP_FPRM) is computed for each 1% RH bin from the CP_Ratio values. The values of CP_FPRM are plotted vs. their bin RH value. The value of RH for CP=0.1 (RHP) and for the turning point CP=0.5 (RHT) are picked off the curve for each temperature regime. Then in the regression equation $CP = (a0\times a1P^{RHP}+a2)P^{-1P}$ set a2=1 (the simple logistic regression $\{1+\exp[b0+b1\cdot RH]\}P^{-1P}$ where a0=exp(b0) and a1=exp(b1), see Wilks, 1995) and solve for first guess values of a0 and a1 using the pair (CP=0.1, RHP) and the pair (CP=0.5, RHT). The 1% RH bins and their computed CP_FPRM values were submitted to a curve-fitting regression algorithm to determine the least-squares best fit values of a0, a1 and a2 given their first-guess values. The best-fit relationship (CP_BF) was superimposed over the CP_Ratio and CP_FPRM curves and is shown in Figure A1. Unlike logistic regression in which CP is guaranteed to lie within the range [0,1], the three-parameter regression is not strictly limited to this range. So CP_BF values were restricted to the [0,1] range in the plots.

Table A1 gives the least-squares best fit values of a0, a1 and a2 for the regression equation $CP = (a0\times a1P^{RHP}+a2)P^{-1P}$ derived from the development soundings and corresponding radar/lidar cloud base and top altitude measurements as described above. These values are used in the regression equation applied to the RAOBs discussed in the accompanying article. For the temperature ranges 5 C > T > -5 C and -35 C > T > -45 C, CP values assigned are temperature-weighted averages of the diagnosed CP values from the respective temperature regimes on either side of 0 C and -40 C boundaries. This insures a smooth transition of the CP values between temperature regimes. Diagnosed values of CP at each report level are then examined, and values of $CP \geq 0.51$ are assumed to denote a cloudy level in the sounding. In this way, cloud top and base altitudes are determined for each diagnosed cloud layer.

Table A1. Coefficients of the nonlinear best fit to CP = (a0×a1P$^{\mathrm{RHP}}$+a2)P$^{\mathrm{-1P}}$ derived from the 19 radiosonde soundings and corresponding radar/lidar cloud base and top altitude measurements taken in 2001 and 2002 at Hanscom Air Force Base, MA. Coefficients are derived separately for the three temperature ranges shown in the table.

Temperature Range	**a0**	**a1**	**a2**
$T \geq 0$ C	3.202991 X 10P$^{\mathrm{6P}}$	8.404975 X 10P$^{\mathrm{-1P}}$	7.947287 X 10P$^{\mathrm{-1P}}$
0 C > T > -40 C	1.2685548 X 10P$^{\mathrm{7P}}$	8.017294 X 10P$^{\mathrm{-1P}}$	9.877875 X 10P$^{\mathrm{-1P}}$
$T \leq -40$ C	3.670042 X 10P$^{\mathrm{3P}}$	8.805682 X 10P$^{\mathrm{-1P}}$	9.612840 X 10P$^{\mathrm{-1P}}$

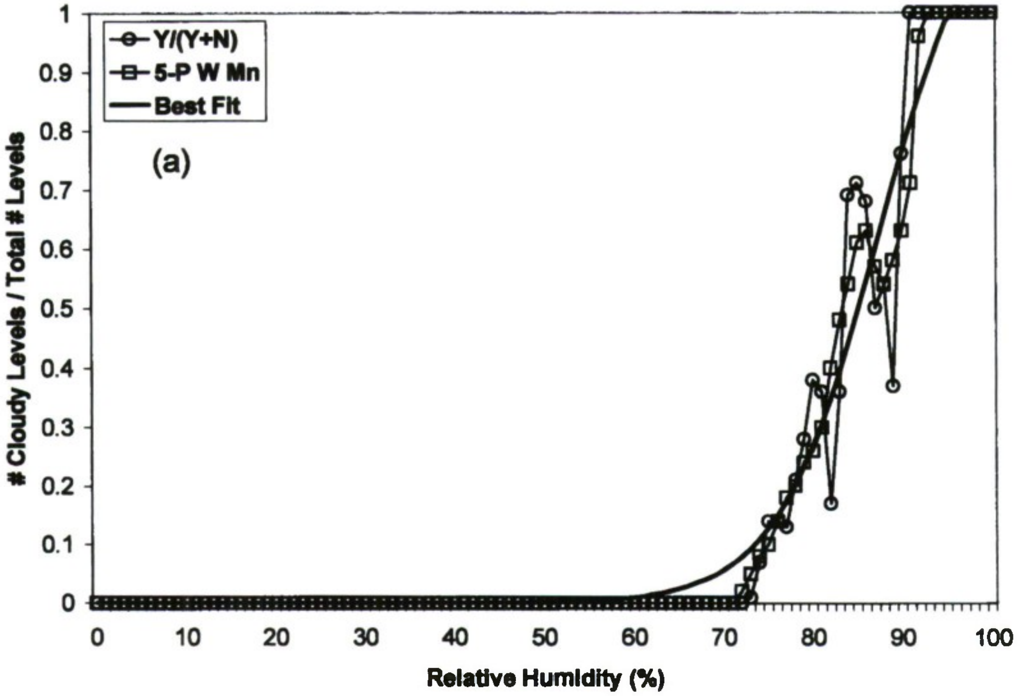
Y/(Y+N)
5-P W Mn
Best Fit
(a)
Cloudy Levels / Total # Levels
0
0.1
0.2
0.3
0.4
0.5
0.6
0.7
0.8
0.9
1
0
10
20
30
40
50
60
70
80
90
100
Relative Humidity (%)

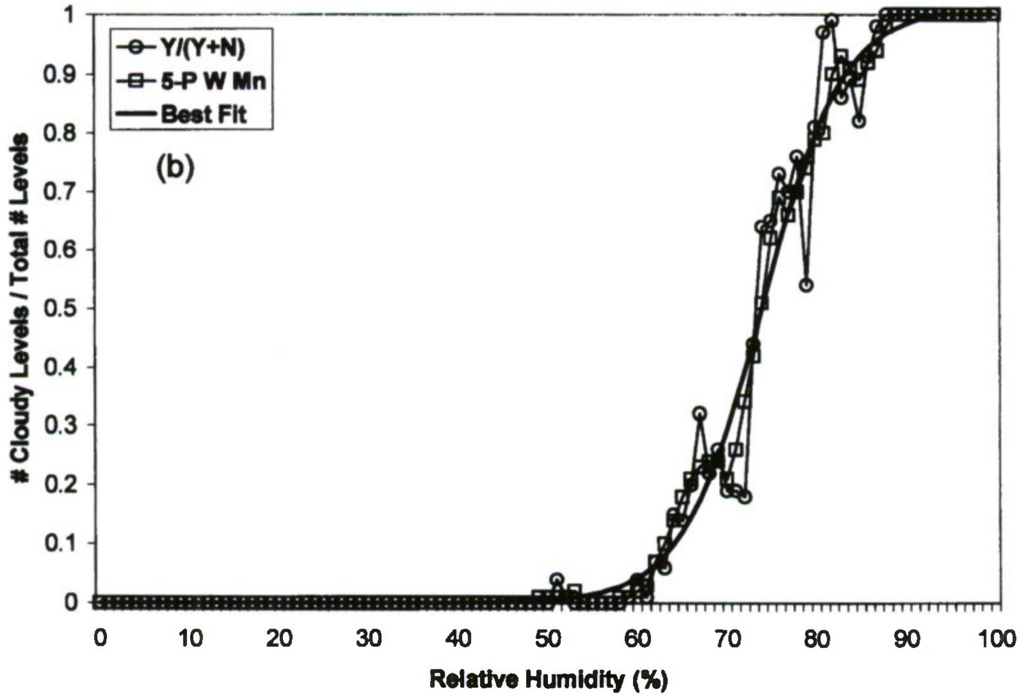
Y/(Y+N)
5-P W Mn
Best Fit
(b)
Cloudy Levels / Total # Levels
0
0.1
0.2
0.3
0.4
0.5
0.6
0.7
0.8
0.9
1
0
10
20
30
40
50
60
70
80
90
100
Relative Humidity (%)

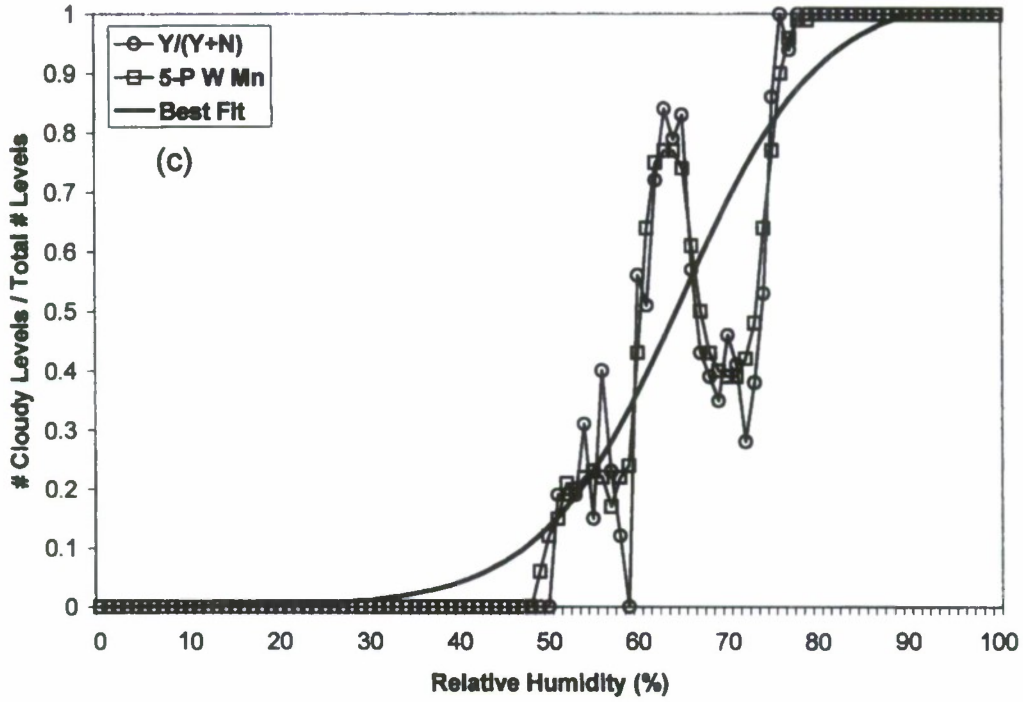

Figure A1. Ratio of number of cloudy report levels to total number of report levels [Y/(Y+N)] for each 1% RH bin, its five-point weighted mean (5-P W Mn) and the nonlinear least squared best fit to the weighted mean (Best Fit) based on 19 co-located radiosonde observations and radar/lidar measurements of cloud layers from various dates in 2001 and 2002 taken at Hanscom Air Force Base, MA. Plots are shown for three different temperature regimes: (a) T ≥ 0 C, (b) 0 C > T > -40 C, and T ≤ -40 C.

References

Beland, R. R., 1993: Propagation through atmospheric optical turbulence. *The Infrared and Electo-Optical Systems Handbook*, Vol. 2, F. G. Smith, Ed., SPIE Engineering Press, 157-232.

Bohren, C. F. and D. R. Huffman, 1983: *Absorption and Scattering of Light by Small Particles.* John Wiley and Sons, 530 pp.

Brown, P. R. A., A. J. Illingworth, A. J. Heymsfield, G. M. McFarquhar, K. A. Browning and M. Gosset, 1995: The role of spaceborne millimeter-wave radar in the global monitoring of ice cloud. *J. Appl. Meteor.*, **34**, 2346-2366.

Chernykh, I. V. and R. E. Eskridge, 1996: Determination of cloud amount and level from radiosonde soundings. *J. Appl. Meteor.*, **35**, 1362-1369.

Clough, S. A., F. X. Kneizys, E. P. Shettle and G. P. Anderson, 1986: Atmospheric radiance and transmittance: FASCOD2. *Proceedings, Sixth Conference on Atmospheric Radiation*, 13-16 May 1986, Williamsburg, VA, Amer. Meteor. Soc., Boston, MA, 141-144.

Desrochers, P. R., 2004: Cloud Optical Depth Retrieval From Cloud Radar and Microwave Radiometer Measurements. AFRL-VS-HA-TR-2004-1193, Environmental Research Papers, No. 1259, Air Force Research Laboratory (AFMC), Hanscom AFB, MA, 21 pp.

Donovan, D. P. and A. C. A. P. van Lammeren, 2001: Cloud effective particle size and water content profile retrievals using combined lidar and radar observations 1. Theory and examples. *J. Geophys. Res.*, **106**, 27425-27448.

Fu, Q., 1996: An accurate parameterization of the solar radiative properties of cirrus clouds for climate models. *J. Climate*, **9**, 2058-2082.

Gustafson, G. B. and R. P. d'Entremont, 2000: Development and Validation of Improved Techniques for Cloud Property Retrieval from Environmental Satellites. AFRL-VS-TR-2001-1549, Air Force Research Laboratory (AFMC), Hanscom AFB, MA, 48 pp. [NTIS ADA 395640.]

Heymsfield, A.J., and C. M. R. Platt, 1975: A parameterization of the particle size spectrum of ice clouds in terms of the ambient temperature and ice water content. *J. Atmos. Sci.,* 41, 846-855.

Jackson, A., 2004: Modified – Dewan Optical Turbulence Parameterizations. AFRL-VS-HA-TR-2004-1116, Environmental Research Papers, No.1259, Air Force Research Laboratory (AFMC), Hanscom AFB, MA, 69 pp.

Jumper, G. Y., and R. R. Beland, 2000: Progress in the understanding and modeling of atmospheric optical turbulence. *Proceedings, 31*PstP *AIAA Plasma Dynamics and Laser Conf.*, 19-22 June 2000, Denver, CO.

Kneizys, F. X., E. P. Shettle, L. W. Abreu, J. H. Chetwynd, G. P. Anderson, W. O. Gallery, J. E. A. Selby, S. A. Clough, 1988: Users Guide to LOWTRAN 7. AFGL-TR-88-0177, Air Force Geophysics Laboratory (AFMC), Hanscom AFB, MA, 137 pp. [NTIS ADA 206773]

Liou, K. N., Y. Takano, S. C. Ou and M. W. Johnson, 2000: Laser transmission through thin cirrus clouds. *Appl. Optics*, **39**, 4886-4894.

McFarquhar, G. M. and A. J. Heymsfield, 1996: Microphysical characteristics of three anvils sampled during the Central Equatorial Pacific Experiment. *J. Atmos. Sci.*, **53**, 2401-2423.

Mozer, J. B. and S. M. Ayer, 1998: Objective techniques for fusion and analysis of mesoscale NWP and satellite-derived cloud data. Proceedings, *Battlespace Atmospheric and Cloud Impacts on Military Operations 1998 Conference*. AFRL-VS-HA-TR-98-0103, Air Force Research Laboratory (AFMC), Hanscom AFB, MA, 57-64. [NTIS ADA 362353]

Norquist, D.C., G.B. Gustafson and R.P. d'Entremont, 2003: Characterizing the geometric properties of clouds from field experiment data sets. Proceedings, *Battlespace Atmospherics and Cloud Impacts on Military Operations 2003 Conference*, Monterey, CA, 2-14, http://www.nrlmry.navy.mil/BACIMO/2003/bacimo.html.

_____, 2005: Cloud layer effects on free space optical communications. Proceedings, *Battlespace Atmospherics and Cloud Impacts on Military Operations 2005 Conference*, Monterey, CA, http://www.nrlmry.navy.mil/BACIMO/2005/Proceedings/.

Ou, S.-C., Y. Takano, K.-N. Liou, R.J. Lefevre and M.W. Johnson, 2002: Laser transmission-backscattering through inhomogeneous cirrus clouds. *Appl. Optics*, **41**, 5744-5754.

Roe, J.M. and W.H. Jasperson, 1980: A new tropopause definition from simultaneous ozone-temperature profiles. AFGL-TR-80-0289, Air Force Geophysics Laboratory (AFSC), Hanscom AFB, MA, 16 pp. [NTIS ADA 091718]

Rothman, L. S. and co-authors, 1998: The HITRAN molecular spectroscopic database and HAWKS (HITRAN Atmospheric Workstation): 1996 edition. *J. Quant. Spect. Rad. Trans.*, **60**, 665-710.

Ruggiero, F. H., D. A. DeBenedictis, R. J. Lefevre, and S. Early, 2004: Mesoscale modeling effects on optical turbulence parameterization performance. Preprints, *20PthP Conf. Weather Analysis and Forecasting and 16PthP Conf. on Numerical Weather Prediction,* 12-15 January 2004, Seattle WA.

Schrader, M. L., W. D. Meyer and C. L. Weaver, 1997: Comments on "A reexamination of the formation of exhaust condensation trails by jet aircraft". J. Appl. Meteor., 36, 623-626.

Wang, J. and W. B. Rossow, 1995: Determination of cloud vertical structure from upper-air observations. *J. Appl. Meteor.*, **34**, 2243-2258.

_____, _____, T. Uttal and M. Rozendaal, 1999: Variability of cloud vertical structure during ASTEX observed from a combination of rawinsonde, radar, ceilometer and satellite. *Mon. Wea. Rev.*, **127**, 2484-2502.

Wilks, D. S., 1995: *Statistical Methods in the Atmospheric Sciences.* Academic Press, 467 pp.

Wylie, D. P., W. P. Menzel, H. M. Woolf, and K. I. Strabala, 1994: Four years of global cirrus cloud statistics using HIRS. *J. Climate,* **7**, 1972-1986.

_____, and _____, 1999: Eight years of high cloud statistics using HIRS. *J. Climate*, **12**, 170-184.